https://doi.org/10.5194/gchron-2022-19
Preprint. Discussion started: 26 July 2022

Chemical Abrasion: The Mechanics of Zircon Dissolution

Alyssa J. McKanna[1], Isabel Koran[1], Blair Schoene[1], and Richard A. Ketcham[2]

[1]*Department of Geosciences, Guyot Hall, Princeton University, Princeton, NJ 08544, USA*
[2]*Jackson School of Geosciences, The University of Texas Austin, Austin, TX 78712, USA*

Correspondence: Alyssa J. McKanna (alyssaa@princeton.edu)

https://doi.org/10.5194/gchron-2022-19
Preprint. Discussion started: 26 July 2022

Abstract

Chemical abrasion is a technique that combines laboratory annealing and partial dissolution in hydrofluoric acid (HF) to selectively remove radiation-damaged portions of zircon crystals prior to U-Pb isotopic analysis, and it is applied ubiquitously to zircon prior to U-Pb isotope dilution thermal ionization mass spectrometry (ID-TIMS). The mechanics of zircon dissolution in HF and the impact of different leaching conditions on the zircon structure, however, are poorly resolved. We present a microstructural investigation that integrates microscale X-ray computed tomography (μCT), scanning electron microscopy, and Raman spectroscopy to evaluate zircon dissolution in HF. We show that μCT is an effective tool for imaging metamictization and complex dissolution networks in three dimensions. We find that most grains do not dissolve predominantly from rim-to-core. Acid frequently reaches crystal interiors via fracture networks spatially associated with radiation damage zoning and inclusions to dissolve higher U zones, material in the vicinity of fractures, and some inclusions. Other acid paths to crystal cores include the dissolution of surface-reaching inclusions and the percolation of acid across zones with high defect densities. In highly crystalline samples dissolution is crystallographically-controlled with dissolution proceeding almost exclusively along the *c*-axis. Increasing the leaching temperature from 180 °C to 210 °C results in deeper etching textures, wider acid paths, more complex internal dissolution networks, and greater volume losses. We discuss the implications of our findings for zircon ID-TIMS U-Pb geochronology and paired trace element analyses, radiation damage annealing models, and for using μCT for imaging radiation damage zoning for (U-Th)/He thermochronology.

https://doi.org/10.5194/gchron-2022-19
Preprint. Discussion started: 26 July 2022

1 Introduction

Zircon U-Pb dating by isotope dilution thermal ionization mass spectrometry (ID-TIMS) produces high-precision dates that the Earth science community depends on to calibrate geologic time (Bowring and Schmidtz, 2003; Schoene, 2014). Zircon crystals affected by radiation damage – caused by alpha recoil events in the ^{238}U, ^{235}U, and ^{232}Th decay series and the spontaneous fission of ^{238}U (Holland and Gottfried 1955; Weber et al., 1990; Murakami et al., 1991; Meldrum et al. 1998; Trachenko et al., 2002; Ewing et al., 2003) – can lose radiogenic Pb by diffusion, leaching, or recrystallization compromising the accuracy of U-Pb ages (Mezger, 1997; Nasdala et al., 1998; Geisler et al., 2002). Pb-loss can sometimes be identified graphically on a concordia diagram when there is a mismatch between the $^{238}U/^{206}Pb$ and the $^{235}U/^{207}Pb$ isotopic clocks, but sometimes discordia lines closely track concordia making Pb-loss difficult to detect, thereby complicating age interpretations from zircon datasets (Mezger, 1997; Schoene, 2014).

Chemical abrasion, a technique that combines laboratory annealing to induce partial structural recovery and leaching in hydrofluoric acid (HF) to selectively remove soluble, radiation-damaged portions of crystals prior to U-Pb isotopic analysis, revolutionized the field's ability to date zircon crystals affected by open system behavior (Mundil et al., 2004; Mattinson, 2005; 2011). Still, many chemically abraded U-Pb zircon datasets exhibit anomalously young, concordant dates that are often attributed to residual Pb-loss (Davydov et al., 2010; Schoene et al., 2010a; Schmidtz and Davydov, 2012; Meyers et al., 2012). Undetected residual Pb-loss can potentially bias critical geologic interpretations such as correlations between terrestrial flood volcanism and biotic crises where ~100 ka precision and accuracy matter (Schoene et al., 2010a), or other correlated biostratigraphic and radioisotopic calibrations constructed to study key climate transitions in Earth history (Schmidtz and Davydov, 2012). This ongoing challenge has recently prompted the ID-TIMS U-Pb community to more closely evaluate how different chemical abrasion protocols – which can vary considerably both within and between individual laboratories – affect geochronological results (Huyskens et al., 2016; Widmann et al., 2019).

Despite the near-universal acceptance of chemical abrasion, the mechanics of zircon dissolution during acid digestion are poorly understood, and several outstanding questions remain. Do most zircon crystals predominantly dissolve from rim to core? How does acid reach crystal interiors to dissolve metamict zones? Does partial dissolution effectively remove all mineral and melt inclusions? How does changing the temperature and duration of leaching affect the zircon structure? It is not unreasonable to assume that a zircon grain predominantly dissolves from rim to core, since crystal rims are often enriched in actinides and radiation damage relative to crystal cores

https://doi.org/10.5194/gchron-2022-19
Preprint. Discussion started: 26 July 2022

(Mattison, 2005; 2011). However, acid has been observed to reach grain interiors presumably via either pre-existing fractures or soluble radiation damage networks formed by interconnected fission or alpha recoil tracks, much like how natural fluids are thought to leach radiogenic Pb from grain interiors (Mundil et al., 2004; Mattinson, 2005; 2011). Despite some qualitative observations, none of these hypotheses have been rigorously tested nor leveraged to gain a mechanistic understanding of the annealing and leaching process.

A basic understanding of the microstructural processes that occur during partial dissolution in HF acid is needed to improve Pb-loss mitigation efforts and ensure the accuracy of high-precision ID-TIMS zircon U-Pb dates. In this study, we present the first three-dimensional (3D) view of zircon dissolution based on microscale X-ray computed tomography data (μCT) acquired before and after leaching in HF. We evaluate both zircon crystals with different radiation damage levels as well as different leaching conditions (180 °C vs. 210 °C, 4 h vs. 12 h). These data are paired with secondary electron images of etched grain surfaces and Raman spectral data used to characterize radiation damage and track changes in zircon crystallinity. In addition to achieving valuable new insights into the mechanics of zircon dissolution, our μCT data reveal exciting opportunities for quickly and non-destructively imaging radiation damage zoning in zircon in 3D which has broader implications for zircon chronology.

2 Methods

2.1 Samples

Our study focuses on four zircon samples (AS3, SAM-47, KR18-04, and BOM2A) that together span nearly the full radiation damage spectrum. AS3 is an intermediate-to-high damage sample from the Mesoproterozoic Duluth Complex anorthositic series, emplaced during the North American Midcontinent Rift (Paces and Miller, 1993; Schmitz et al., 2003; Takehara et al., 2018; Swanson-Hysell et al., 2020). The sample of AS3 used in this study is the same as that studied by Takehara et al. (2018) which was collected from the same locality as that of Paces and Miller (1993) (92°09′32.4″, 46°45′43.4″). AS3 crystals are coarse-grained, orange to orangish-brown, and fractured. Most grains are tabular prisms or anhedral shards and many show evidence of hydrothermal alteration (Takehara et al., 2018). SAM-47 is an intermediate-to-high damage Archean sample from the Corunna Downs granitoid complex of the Pilbara Craton (89°59′55.97″, 100°08′2.38″). Grains are euhedral, brown, and translucent. KR18-04 is an intermediate-to-low damage sample from a Neoproterozoic rhyolite body associated with the glaciolacustrine Konnarock Formation of Virginia, USA (MacLennan et al., 2020) (36°41'47.95", 81°24'22.08"). Grains are small, transparent, pink-

https://doi.org/10.5194/gchron-2022-19
Preprint. Discussion started: 26 July 2022

orange and prismatic. BOM2A is our lowest-damage sample from a Paleocene trachyte dike in Mumbai, India associated with rifting following the main phase of Deccan Traps volcanism (Basu et al., 2020). Crystals are small, transparent, colorless, and prismatic.

Aliquots of unannealed and annealed (900 °C for 48hr) grains from each of the four zircon samples were set aside at the start of the study, mounted, polished, and characterized using Raman spectroscopy to quantify the degree of radiation damage present in each sample, as key bands in the zircon Raman spectrum broaden predictably with increasing damage (Nasdala et al., 2001; Palenik et al., 2003; Váczi and Nasdala, 2017). Annealed grain mounts were also imaged using optical microscopy, cathodoluminescence (CL) imaging, and/or backscattered electron (BSE) imaging to characterize growth textures for each sample (Fig. 1).

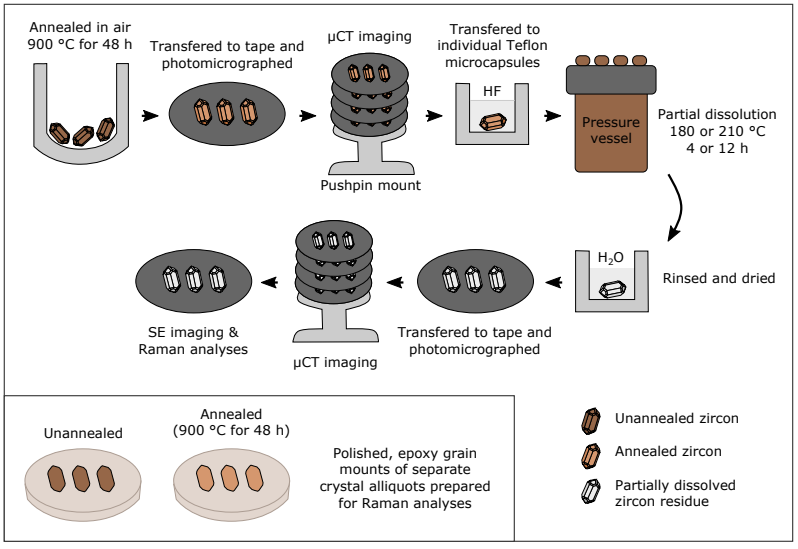

Figure 1: Summary of our experimental workflow.

2.2 Workflow for partial dissolution experiments

A diagram depicting our experimental workflow is presented in Fig. 1. Separate aliquots of the four zircon samples were annealed in quartz crucibles in air at 900 °C for 48 hours in a box furnace. Annealed grains were mounted on sticky tape (~6 mm diameter circles fashioned using a hole punch) and imaged using optical microscopy. The four sticky tape mounts were then stacked on top of a pushpin and loosely secured with tape for µCT imaging (Cooperdock et al., 2016,). After imaging, grains were removed from the sticky tape and transferred to individual Teflon microcapsules for leaching in concentrated HF in a Parr Instrument Company pressure digestion vessel at 180 °C or 210 °C for a duration of 4 or 12 h. The chosen temperatures bracket the range

https://doi.org/10.5194/gchron-2022-19
Preprint. Discussion started: 26 July 2022

commonly used for chemical abrasion by the ID-TIMS U-Pb community (Huyskens et al., 2016; Widmann et al., 2019). Leaching durations were selected based on a sample's initial radiation damage content. Most intermediate-to-high damage zircon crystals (AS3 and SAM-47) were chemically abraded at shorter durations to ensure that intact zircon residues remained (as opposed to dust), although one subset of AS3 grains were leached at 180 °C for the full 12 h. The intermediate-to-low damage samples (KR18-04 and BOM2A) maintained structural integrity over longer leaching durations, so grains were leached for the full 12 h period commonly used for chemical abrasion.

After partial dissolution, residues – the portions of zircon crystals that survive chemical abrasion – were rinsed in Milli-Q water, dried down, and carefully transferred to fresh sticky tape. Mounted residues were then re-imaged using optical microscopy and µCT to generate a "before" and "after" imagery dataset. Microphotographs of annealed grains and chemically abraded zircon residues are presented in Fig. 2. Following µCT, residue mounts were carbon coated, and secondary electron (SE) images of residue surfaces were acquired using a scanning electron microscope (SEM). Raman spectra were measured for a subset of zircon residues to characterize samples' crystallinities.

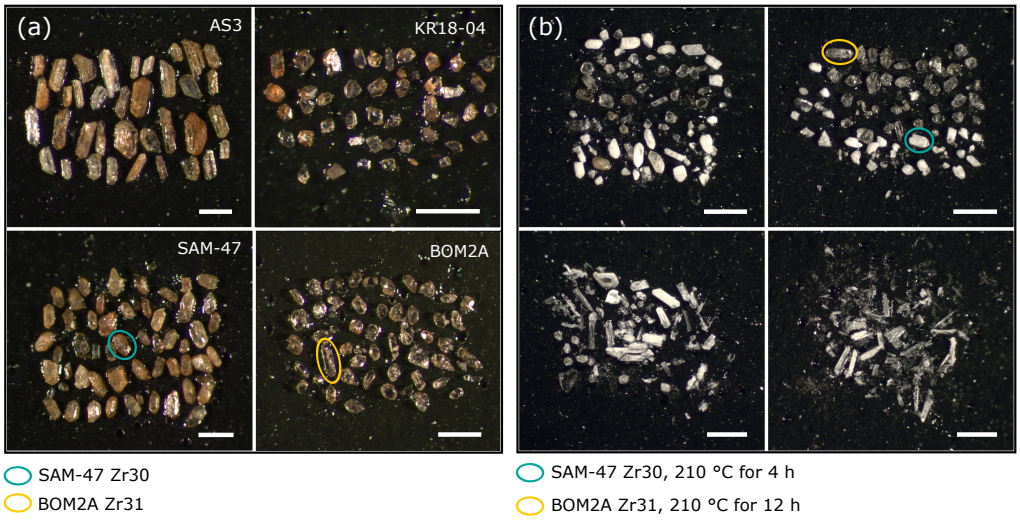

Figure 2: Photomicrographs of zircon crystals mounted on tape for µCT imaging. **(a)** Photomicrograph of annealed grains prior to chemical abrasion **(b)** Photomicrograph of chemically abraded zircon residues. Each tape mount in this image has a mixture of different zircon samples treated at different leaching conditions.

https://doi.org/10.5194/gchron-2022-19
Preprint. Discussion started: 26 July 2022

2.3 Instrumentation and analyses

Chemical abrasion was carried out using equipment and clean lab space at Princeton University. CL and BSE electron images of polished mounts were acquired using the XL30 FEG SEM at the PRISM Imaging and Analysis Center at Princeton University equipped with a mini-Gatan CL detector and a semiconductor BSE detector. Most images were acquired using a 10 kV accelerating voltage, 10 mm working distance, and spot size 5. SE images of chemically abraded zircon residues were captured using the Quanta FEG 200 Environmental-SEM also at the PRISM Imaging and Analysis Center. This system is equipped with a Schottky field emission gun and Everhart-Thornley secondary electron detector. SE images were acquired using low vacuum mode (~0.4 to 0.8 Torr) to minimize charging due to sample topography. Scans used a 10 kV accelerating voltage, 10 to 10.5 mm working distance, and spot size 4 or 5.

All X-ray computed tomography data were collected at the High-Resolution X-ray Computed Tomography Facility at the University of Texas at Austin using a Zeiss Xradia 620 Versa. Measurements were made with X-rays set to 120 kV and 15 W and prefiltered with the LE3 filter. For each scan 2401 views were obtained over a 360° rotation at 4 s per view on the 4x detector. 16-bit TIFF images were reconstructed at 1.62 μm/voxel, using a beam hardening correction setting of 1.8 in the Xradia Reconstructor software. All 2D and 3D visualizations presented were rendered using Object Research Systems (ORS) Dragonfly software.

Raman spectra were acquired using the Horiba LabRAM Evolution Raman spectrometer in the High-Pressure Mineral Physics Laboratory at Princeton University. This confocal system is equipped with 532 nm and 632.81 nm diode lasers and a thermoelectrically cooled CCD detector. The instrument was calibrated daily using the silicon 520.7 cm^{-1} Raman band and the automated protocol implemented within the Horiba Scientific LabSpec6 software. Additionally, a quartz reference spectrum was acquired daily to verify the accuracy of measured peak positions. All measurements were made using an 1800 g/mm grating, a 100 μm slit, and a 400 to 100 μm confocal pin hole. This setup has a spectral resolution better than 2 cm^{-1} and a spatial resolution of ~2 μm. Polynomial background subtractions and Gaussian-Lorentzian peak fits were made using LabSpec6 software. Peak widths have estimated uncertainties on the order of 10% (2σ) based on tests of measurement and peak fit reproducibility. All reported peak widths (full width at half maximum, FWHM) have been corrected for instrumental broadening following the approach of Váczi (2014).

3 Results

https://doi.org/10.5194/gchron-2022-19
Preprint. Discussion started: 26 July 2022

3.1 Images of polished grain mounts

SEM and reflected light images of annealed AS3 and SAM-47 grains are presented in Fig. 3. CL images of AS3 grains reveal broad oscillatory or convoluted compositional zoning patterns with evidence of hydrothermal alteration. Many crystals are finely fractured, and some have large melt inclusions that are commonly oriented parallel to the *c*-axis. Some fractures and alteration zones are observed to cross-cut compositional zones. SAM-47 crystals were not CL luminescent. Reflected light images acquired under the Raman microscope, however, show that most grains have fine-scale concentric growth zoning. BSE images reveal that some crystals are finely fractured and host inclusions. Many of these inclusions are cross-cut by fractures. SEM images of annealed KR18-04 and BOM2A zircon grains are presented in Fig. 4. Both samples have typical magmatic growth patterns including some oscillatory zoning and some faint, broad

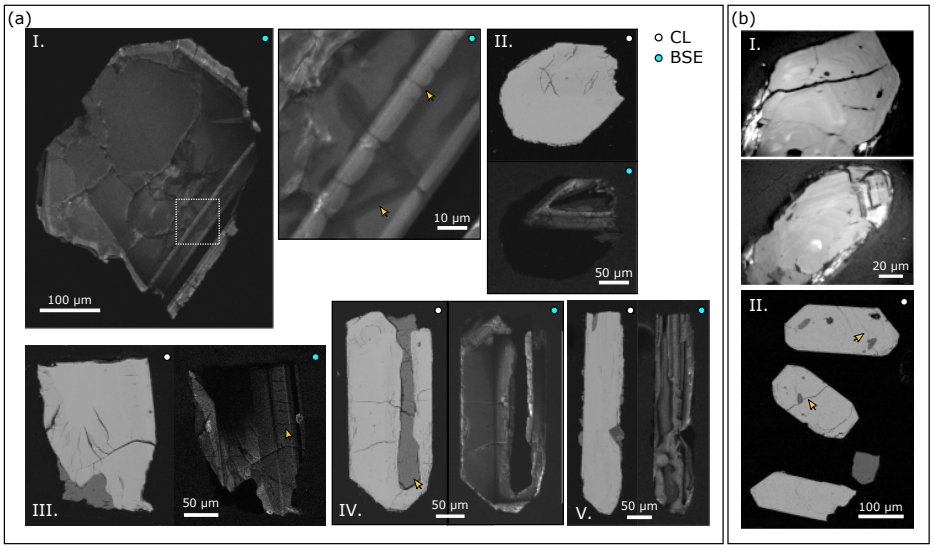

Figure 3: Representative images of annealed AS3 and SAM-47 zircon that have not been treated by chemical abrasion. **(a)** SEM images of annealed AS3 zircon. I. A zircon with simple growth zoning. Arrows highlight dark hydrothermal alteration zones associated with fine-scale fractures. Some fractures cross-cut compositional zones. II. Zircon with an unfractured metamict rim and a fractured core. III. Zircon with row of fractures that cross-cuts a compositional zone. IV. Zircon with a large melt inclusion oriented parallel to the c-axis. V. Zircon with convolute growth zoning. **(b)** Representative images of annealed SAM-47 zircon. I. Reflected light images showing fine-scale concentric growth zoning. II. BSE images showing that some grains are finely fractured. Some of these fractures pass though mineral inclusions (arrows).

https://doi.org/10.5194/gchron-2022-19
Preprint. Discussion started: 26 July 2022

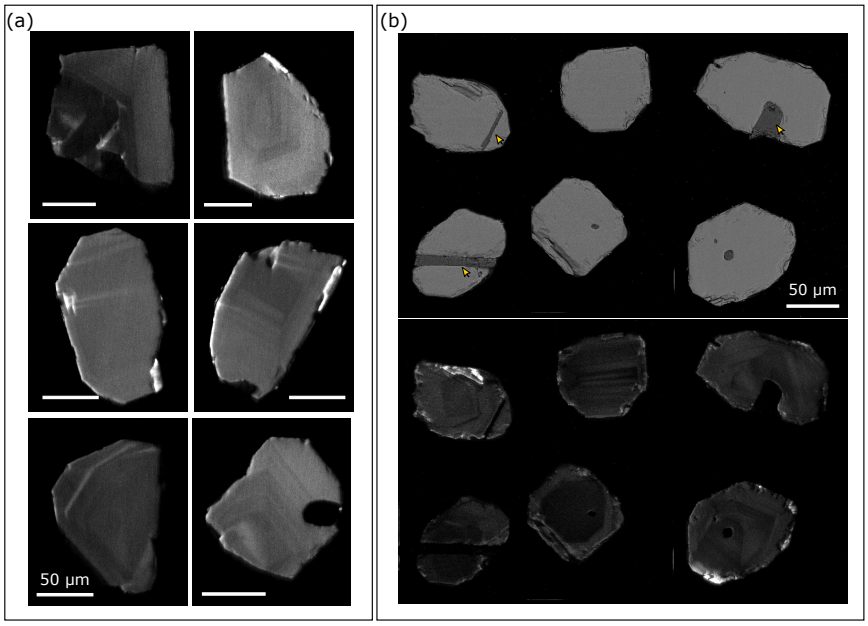

Figure 4: Representative images of annealed KR18-04 and BOM2A zircon that have not been treated by chemical abrasion. **(a)** CL images of annealed KR18-04 zircon with typical magmatic growth patterns. All scall bars are 50 µm. **(b)** Representative BSE (top) and CL (bottom) images of annealed BOM2A zircon showing typical magmatic growth zoning. Arrows highlight the frequent occurrence of apatite inclusions.

zones. Fractures are rare. BOM2A crystals frequently have needle-like apatite inclusions, many of which are surface reaching.

3.2 Raman spectroscopy

3.2.1 Polished grain mounts

Key bands in the zircon Raman spectrum – most notably the $\upsilon_3(SiO_4)$ Si-O asymmetric stretching band near ~1008 cm^{-1} and the external E_g mode near ~357 cm^{-1} – broaden and shift to lower frequencies with increasing radiation damage (Nasdala et al. 1995, Zhang et al. 2000, Nasdala et al. 2001, Anderson et al. 2020a, Härtel et al. 2021). Measured $\upsilon_3(SiO_4)$ and E_g peak widths and positions are reported in Table S1. We derive alpha dose estimates (α/g) for each sample using the calibration presented by Váczi and Nasdala (2017) for the $\upsilon_3(SiO_4)$ peak width.

Raman data for unannealed AS3 and SAM-47 indicate intermediate-to-high degrees of radiation damage with strong inter- and intra-crystalline variations (Fig. 5a). Estimated

https://doi.org/10.5194/gchron-2022-19
Preprint. Discussion started: 26 July 2022

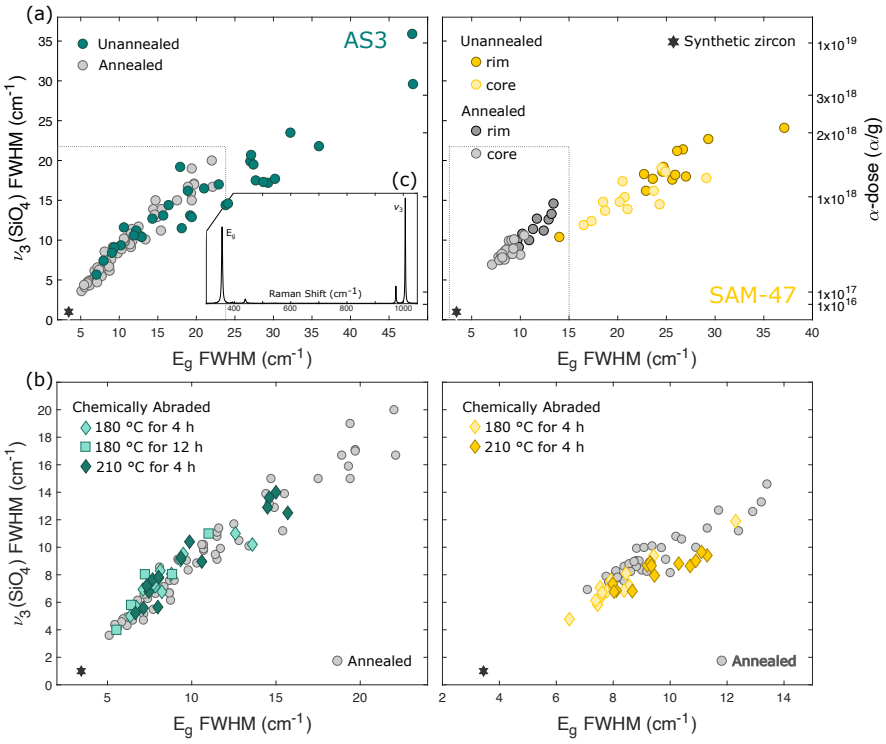

Figure 5: Raman $v_3(SiO_4)$ and E_g peak width data for intermediate-to-high damage samples AS3 (left) and SAM-47 (right). **(a)** Results for unannealed and annealed (900 °C for 48 hour) zircon samples. Alpha dose estimates for unannealed zircon samples derived from $v_3(SiO_4)$ peak width measurements are shown on the right y-axis (Váczi and Nasdala, 2017). Gray boxes mark the plot area presented in (b). **(b)** Results for annealed zircon samples and chemically abraded zircon residues. **(c)** Representative spectrum of synthetic zircon with peak assignments.

alpha doses for AS3 range from ~2×10^{17} α/g to >1×10^{19} α/g (the saturation value for Raman-derived damage estimates). CL black regions that yielded anomalous zircon spectra with fluorescent artifacts indicative of altered material were excluded from radiation damage estimates. Estimated alpha doses for unannealed SAM-47 samples range from ~6×10^{17} α/g to 2×10^{18} α/g. Crystal rims in SAM-47 samples have accumulated more radiation damage than crystal cores, indicating that rims are enriched in actinides relative to cores. Alpha dose estimates for both AS3 and SAM-47 span above and below the estimated alpha dose threshold assigned to fission track percolation 1.9×10^{18} α/g (Ketcham et al., 2013). This threshold also corresponds to key transitions in zircon material properties including density (Holland and Gottfried, 1955; Murakami et al., 1991; Ewing et al., 2003). Unannealed KR18-04 and BOM2A zircon samples have low-to-intermediate levels of radiation damage and a lesser degree of radiation damage zoning (Fig. 6a). Estimated alpha doses range from ~5×10^{16} to 7×10^{17}

https://doi.org/10.5194/gchron-2022-19
Preprint. Discussion started: 26 July 2022

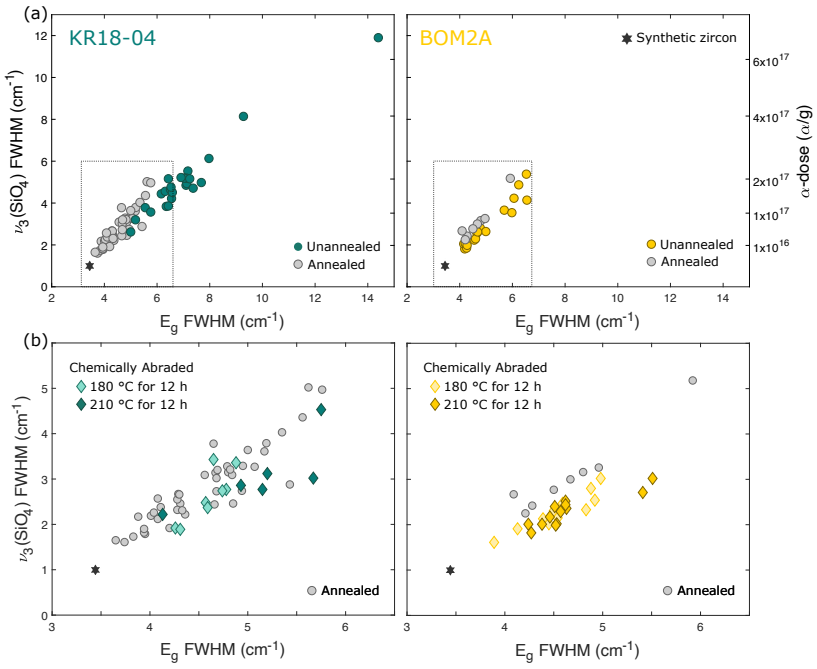

Figure 6: Raman $\nu_3(SiO_4)$ and E_g peak width data for lower damage samples KR18-04 (left) and BOM2A (right). **(a)** Results for unannealed and annealed (900 °C for 48 hour) zircon samples. Alpha dose estimates for unannealed zircon samples derived from $\nu_3(SiO_4)$ peak width measurements are shown on the right y-axis (Váczi and Nasdala, 2017). Gray boxes mark the plot area presented in (b). **(b)** Results for annealed zircon samples and chemically abraded zircon residues.

α/g and ~6×10^{15} to 2×10^{17} α/g for the two samples, respectively, well below the 1.9×10^{18} α/g threshold.

Compared to their unannealed counterparts, $\nu_3(SiO_4)$ and E_g peak widths in annealed AS3, SAM-47, and KR18-04 samples are narrower, consistent with the partial annealing of radiation damage (Fig. 5a and Fig. 6a) (Zhang et al., 2000; Geisler et al., 2002; Ginster et al., 2019; Härtel et al., 2021). $\nu_3(SiO_4)$ and E_g peak width ranges for each sample have also narrowed, implying that annealing has decreased the magnitude of inter- and intra-crystalline variations in radiation damage. Annealing seems to have had minimal effect on the crystallinity of low-damage BOM2A. We note that none of the samples have achieved complete structural recovery after annealing at 900 °C for 48 h, since all measured peak widths are broader than that of synthetic zircon.

We note that relationship between the $\nu_3(SiO_4)$ and E_g peak widths is steeper after annealing in each of the four samples, since the two Raman peaks have different temperature sensitivities (Härtel et al., 2021). This observation suggests that laboratory

https://doi.org/10.5194/gchron-2022-19
Preprint. Discussion started: 26 July 2022

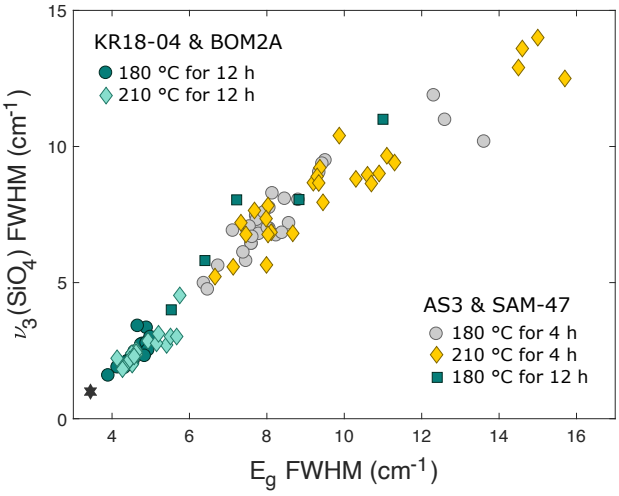

Figure 7: Raman $\nu_3(SiO_4)$ and E_g peak width results for all chemically abraded zircon residues.

annealing is not simply the inverse of radiation damage accumulation. As such, we caution against using the Váczi and Nasdala (2017) calibration to derive alpha dose estimates from $\nu_3(SiO_4)$ peak widths for annealed or chemically abraded samples and omit alpha dose axes from Figures 5b and 6b.

3.2.2 Chemically abraded zircon residues

Raman $\nu_3(SiO_4)$ and E_g peak width measurements for chemically abraded zircon residues are shown in Fig. 5b and Fig. 6b. The broadest peaks for AS3, SAM-47, KR18-04, and BOM2A residues are narrower than that of their annealed but unleached counterparts. This pattern is most evident in the two higher damage samples, indicating that HF leaching has dissolved the most damaged zircon material in each sample. The two lower damage samples, however, each have only one annealed datapoint with a broader $\nu_3(SiO_4)$ and E_g peak. We interpret this to suggest that small differences in radiation damage in crystals with low initial alpha doses does not have a significant impact on which portions of a grain dissolve.

Notably, SAM-47 and BOM2A residues each have at least one data point with a narrower $\nu_3(SiO_4)$ and E_g peak width than their solely annealed counterparts suggesting that some residues have a higher degree of crystallinity. Further, we find that the residue datapoints for these two samples largely plot below (at lower ν_3 for a given E_g) the annealed datapoints indicating a change in the relationship between the $\nu_3(SiO_4)$ and E_g peaks. Taken together, these observations could suggest that additional structural recovery occurs in some zircon samples during HF leaching even after dry annealing at significantly higher temperatures.

https://doi.org/10.5194/gchron-2022-19
Preprint. Discussion started: 26 July 2022

In Fig. 7 we compile Raman results for the four zircon samples to evaluate the effects of different partial dissolution conditions on the crystallinity of zircon residues. The spread in datapoints for AS3 residues leached at 180 °C for 12 h (all SAM-47 zircons disintegrated after 12 h) is shifted toward narrower values compared to AS3 and SAM-47 residues leached at either 180 °C or 210 °C for 4 h. This could imply that increasing the duration of the leaching step results in a more crystalline zircon residue due to the progressive dissolution of higher damage domains. We note, however, that only a small number of AS3 crystals survived 12 h of chemical abrasion, and only a small number of Raman analyses were made. We recommend further study to better evaluate this possibility. Somewhat surprisingly, we do not find leaching temperature to have a significant effect on the crystallinity of zircon residues; AS3 and SAM-47 samples leached for 4 h at 180 °C or 210 °C have residues with broadly similar peak width distributions, as do KR18-04 and BOM2A samples leached for 12 h at 180 °C or 210 °C. This could potentially reflect a small n-problem. We find that AS3 residues leached at 180 °C for 12 h have universally broader peak widths compared to KR18-04 and BOM2A residues treated under the same leaching conditions. These results stress that a sample's initial radiation damage content profoundly affects the crystallinity of a sample's residue.

3.3 Imaging textures before and after partial dissolution

3.3.1 AS3

The accumulation of radiation damage decreases the density of zircon by 17% from ~4.7 to 3.9 g/cm^3 with the most rapid density change occurring over an alpha dose interval of ~1×10^{18} to ~4×10^{18} α/g (Holland and Gottfried, 1955; Murakami et al., 1991; Ewing et al., 2003; Nasdala et al., 2004). Raman data for unannealed AS3 grains indicates that these samples have alpha doses spanning above and below this interval. Lower density materials attenuate X-rays less, so metamict zones should appear darker in grayscale μCT image slices than crystalline zircon. Indeed, we find that some AS3 crystals exhibit density zoning (Fig. 8), indicating that annealing at 900 °C for 48 hr does not significantly increase zircon density in strongly metamict material. As evidenced by our SE images and discussed further below, μCT does not capture radiation damage zoning that does not result in a strong density contrast such as variations in radiation damage below the ~1×10^{18} α/g threshold.

https://doi.org/10.5194/gchron-2022-19
Preprint. Discussion started: 26 July 2022

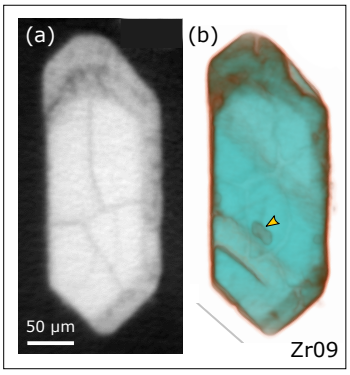

Figure 8: µCT images of a zircon with density zoning. **(a)** 2D µCT image slice of an annealed – but not leached – AS3 zircon crystal with a dark, low-density rim interpreted as metamict and a light, crystalline, and fractured core. **(b)** Semi-transparent 3D rendering of the µCT data for the same grain. High-density zircon is teal, and lower-density material is orange-brown. The arrow marks an interior inclusion. The faint stripes are surface indents of surficial inclusions not shown.

Images of annealed and chemically abraded AS3 grains are presented in Figures 9, 10, 11, S1, and S2. Each figure shows results for one of the three leaching conditions – 180 °C for 4 h, 210 °C for 4 h, and 180 °C for 12 h –, respectively. Here we briefly summarize key observations. We refer the reader to the figure captions for additional context.

Damaged zircon is intrinsically more soluble in HF than crystalline zircon. µCT images show that low-density metamict rims and interior zones are removed early in the leaching process at relatively low temperatures (180 °C for 4 h). SE images also document the removal of fine-scale compositional zones early in the leaching process.

Etching in SE images reflect the removal of soluble crystal defects including defects related to partially-annealed radiation damage, dislocations, low-angle grain boundaries, and intrinsic point defects. For spatial reference, fission tracks are ~16.7 µm and alpha recoil tracks (clusters of alpha recoil tracks stemming from a single decay chain) average ~125 nm in length prior to annealing (Ewing et al., 2003; Jonckheere, 2003). In SE images, low damage compositional zones have smooth surfaces, whereas higher damage zones have pitted or sponge-like surfaces due to the etching of closely spaced radiation damage defects (Fig. 9c and Fig. 10aI). Etch pits and radiation damage zoning textures are not observed in µCT images due to the dataset's lower spatial resolution (1.62 µm voxels).

The geometric shape of individual etch pits on a grain's surface – such as the diamond or pyramid-like appearance of many pits – is independent of the nature of the defect (Jonckheere and Van den haute, 1996; Jonckheere et al., 2005; 2022). The pit's surface

https://doi.org/10.5194/gchron-2022-19
Preprint. Discussion started: 26 July 2022

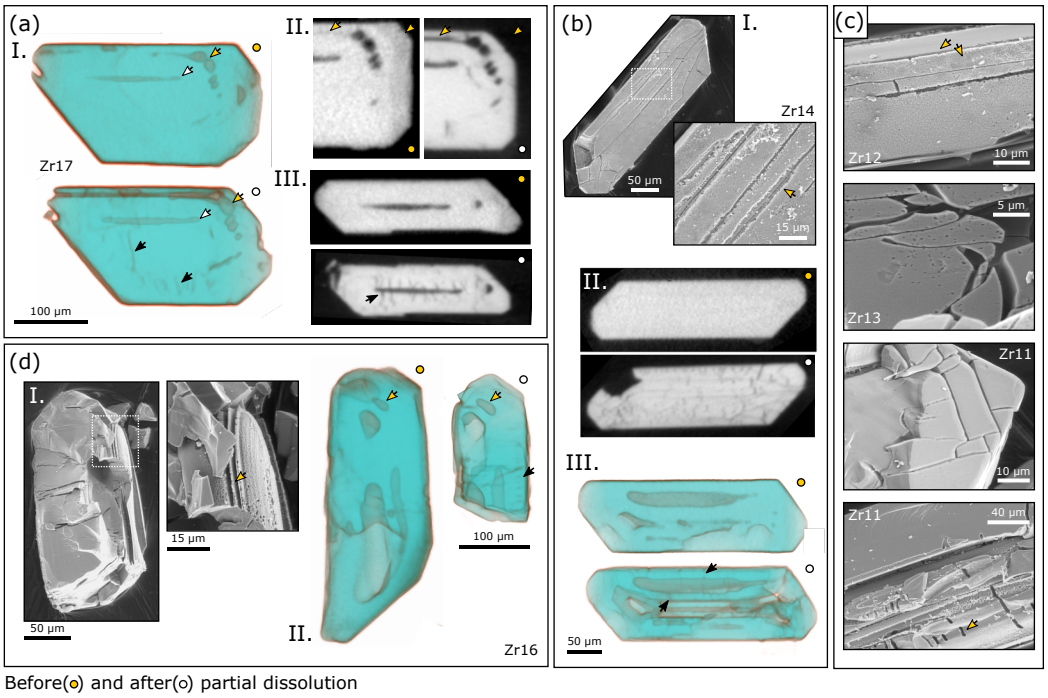

Figure 9: SE and µCT images of AS3 grains pre- and post-chemical abrasion (yellow dots and white dots, respectively) at 180 °C for 4 h. **(a)** I. Semi-transparent 3D renderings of µCT data for Zr17 showing melt inclusions removed by partial dissolution (yellow and white arrows) and newly visible fractures (black arrows). II. 2D µCT image slices showing the removal of a metamict rim and interior compositional zone. III. 2D µCT cross section of the melt inclusion marked by white arrows in I. Newly visible radial fractures have developed along the length of the melt inclusion (black arrow). **(b)** I. SE images of Zr14 showing the widening of fractures on the grain surface. II. 2D µCT image slices showing a fracture network after partial dissolution. III. 3D rendering of µCT data showing radial fractures (black arrows) around large melt inclusions removed by partial dissolution. **(c)** SE images of zircon residues illustrating the contrast between a smooth, low damage surface and a higher damage pitted surface (Zr12), curved acid paths and small etch pits (Zr13), blocky fractures (Zr11 top), and dumbbell-like dissolution features (Zr11 bottom). **(d)** I. SE images of Zr16 showing the removal of fine-scale compositional zones. II. 3D rendering of µCT data with showing the removal of large melt inclusions (yellow arrows), the formation of a parallel fracture sequence (black arrow), and significant volume loss likely due to breakage along the grain center where there are two giant melt inclusions.

symmetry instead reflects the mineral's crystallography. Zircon dissolution in HF is anisotropic, so the shape of etch pits also varies with crystallographic orientation (Gleadow et al., 1976; Yamada et al., 1995). As such, while individual diamond-shaped etch pits closely resemble SE images of etched fission tracks presented by others for zircon, apatite, monazite, and titanite (e.g., Jones et al., 2022), these could reflect other defect types such as lattice dislocations; if the surficial etch pit has overtaken the initial

https://doi.org/10.5194/gchron-2022-19
Preprint. Discussion started: 26 July 2022

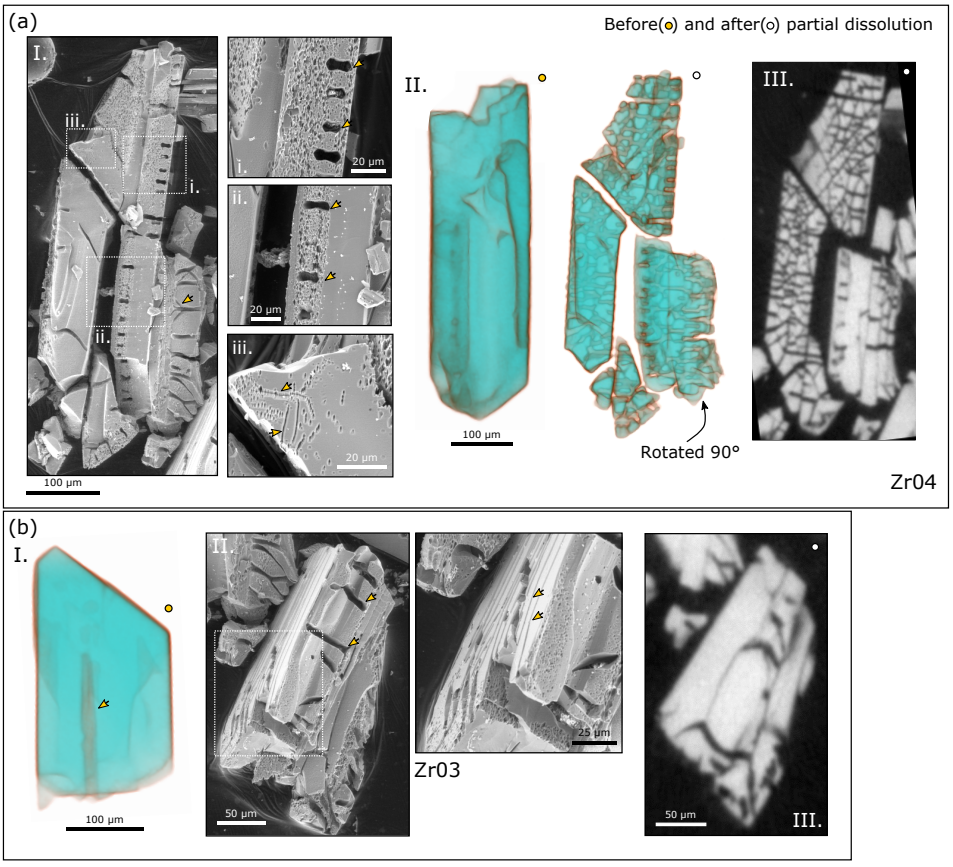

Figure 10: SE and µCT images of AS3 grains pre- and post-chemical abrasion at 210 °C for 4 h. **(a)** I. SE images of Zr04, a large crystal broken into four pieces. The rotated piece marked with a yellow arrow shows a nice cross-section of the grain interior. The arrow highlights an example of a branching channel. The higher magnification images show that these channels correlate with dumbbell features that cross-cut compositional zones of relatively low (i) or high (ii) radiation damage. iii shows etch pit arrays likely indicative of dislocations loops or low-angle grain boundaries. II. 3D rendering of the µCT data shows the development of a complex dissolution network in the crystal's interior. III. 2D µCT image slice showing that the intensive fracturing observed in 3D is restricted to narrow plane within the crystal. **(b)** I. Semi-transparent 3D rendering of µCT data for Zr03 showing a large melt inclusion. II. SE images show elongated, channel-like dumbbells (low magnification) and the apparent removal of fine-scale compositional zones (high magnification). III. 2D µCT image slice showing wide acid paths in the grain interior.

fission track channel beneath the surface it is impossible to tell. Most fission tracks likely annealed during our pre-leach 900 °C annealing step (e.g., Yamada et al. 1995), although some etch pits could reflect fission tracks that were pre-etched geologically prior to chemical abrasion. Given the limited abundance, larger size, and spacing of the

https://doi.org/10.5194/gchron-2022-19
Preprint. Discussion started: 26 July 2022

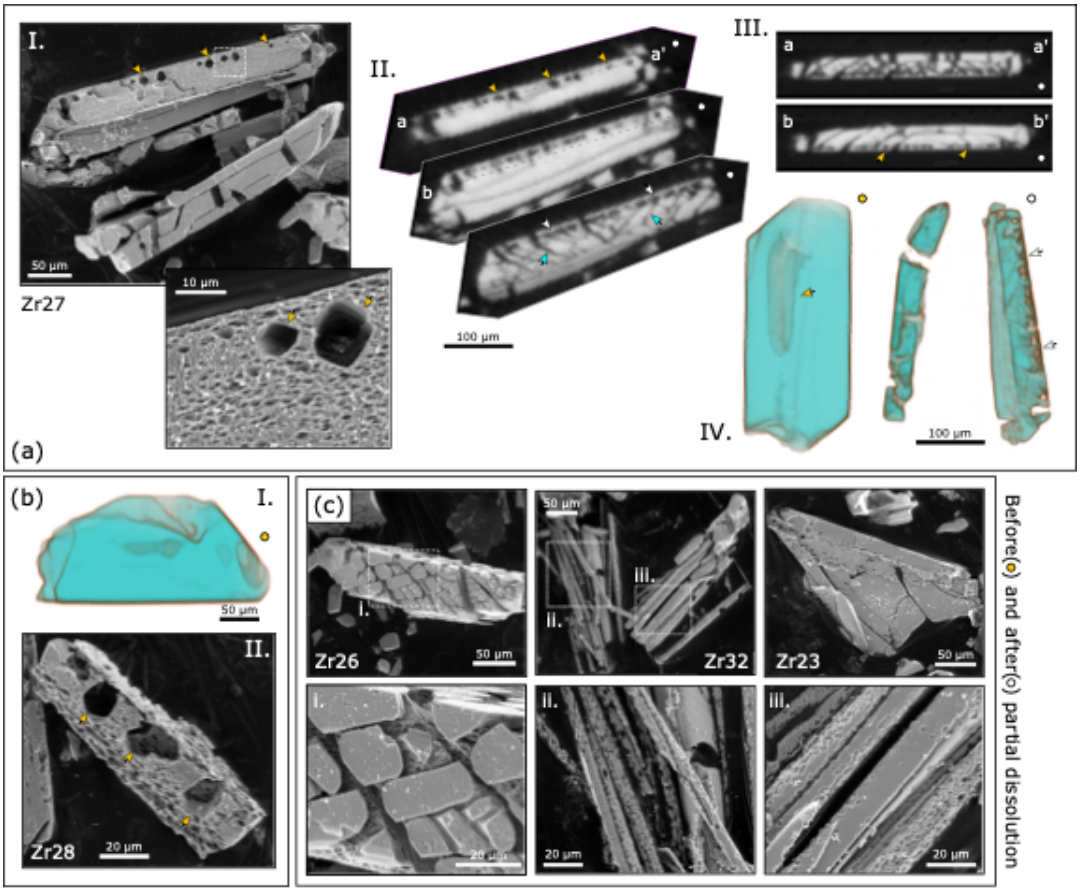

Figure 11. SE and µCT images of AS3 pre- and post-chemical abrasion at 180 °C for 12 h. **(a)** I. SE images of sample Zr27 showing a row of dumbbells along the length of the zircon crystal. The higher magnification SE image shows a sponge-like surface texture. II. A series of 2D µCT image slices progressively stepping down to view structures beneath the crystal's surface. The yellow arrows highlight the same dumbbell features marked on the SE image in I. The teal arrows highlight fractures, many of which radiate from dumbbell features. The white arrows mark another series of dumbbells on the bottom side of the crystal. III. Cross-sectional 2D µCT image slices of a-a′ and b-b′ as labeled in II. White arrows mark second set of dumbbells with a different crystallographic orientation. IV. Semi-transparent 3D rendering of µCT data with arrows highlighting a large melt inclusion. The dissolution of this inclusion likely caused the grain to break into two pieces. The white arrows mark the same row of dumbbells as indicated by the white arrows in II. **(b)** I. Semi-transparent 3D rendering of µCT data for Zr28 prior. II. SE image of the husk-like zircon shell with large dumbbell features. **(c)** SE images of zircon residues Zr26, Zr32, and Zr23 showing cobble stone, straw, and lace-like textures.

diamond and pyramid-like etch pits, we find them unlikely to reflect etching of partially annealed-alpha recoil tracks. We interpret etch pit arrays that do not correlate

https://doi.org/10.5194/gchron-2022-19
Preprint. Discussion started: 26 July 2022

with expected compositional zoning patterns (Fig. 10a-iii) to reflect the dissolution of dislocation loops or low-angle grain boundaries.

Etch textures are more subtle at low temperatures and short leaching durations. At hotter temperatures and longer leaching durations, etched zones have deeper, sponge-like textures indicative of a greater degree of dissolution. At a full 12 h leach, only a heavily dissected crystalline husk, a collection of perforated straw-like zones, or a cobble stone-like residue is sometimes all that remains.

Geometrical dissolution features that cross-cut compositional zones as highlighted in Fig. 10a and Fig. 11a and hereafter referred to as dumbbells, are a common feature in AS3 zircon residues. Some dumbbells cross-cut zones of relatively high radiation damage, while others cross-cut zones of relatively low radiation damage. All observed dumbbells are oriented parallel to the grain's *c*-axis. 3D rendering of μCT data reveal that dumbbells are surface expressions of complex, fracture networks restricted to specific compositional zones. The geometrical shape of dumbbells and the branching, channel-like appearance of some fractures in SE imaging, indicate that these fracture networks are focal points for crystallographically-controlled dissolution. Aside from dumbbells, we note that fractures in general are a common feature in both SE and μCT images of leached grains.

Excitingly, our μCT dataset also generates new insights into the fate of inclusions hosted deep within grain interiors. In μCT image slices, inclusions appear dark with grayscale intensities marginally above that of background (air and tape) due to their low density and mean atomic number relative to that of zircon. We interpret an inclusion to have been removed if: 1) its gray-scale intensity decreases to that of background, 2) there is a change to its size or morphology after leaching, or 3) there is a clear acid path to the inclusion. We find that the majority of inclusions in AS3 appear to dissolve at short leaching durations. Around the largest inclusions, we observe radial fractures in μCT images of leached grains that are not apparent in the before imagery dataset.

3.3.2 SAM-47

Images of annealed and chemically abraded SAM-47 grains treated at 180 °C or 210 °C for 4 h are presented in Figures 12, 13, S3, and S4. Like AS3, several annealed SAM-47 crystals have density zoning in μCT. In most cases density zoning is in the form of metamict rims, however, we note that one crystal was seen with oscillatory density zoning. This finding is consistent with our Raman data which shows that unannealed SAM-47 samples have alpha doses that span the interval over which density changes

https://doi.org/10.5194/gchron-2022-19
Preprint. Discussion started: 26 July 2022

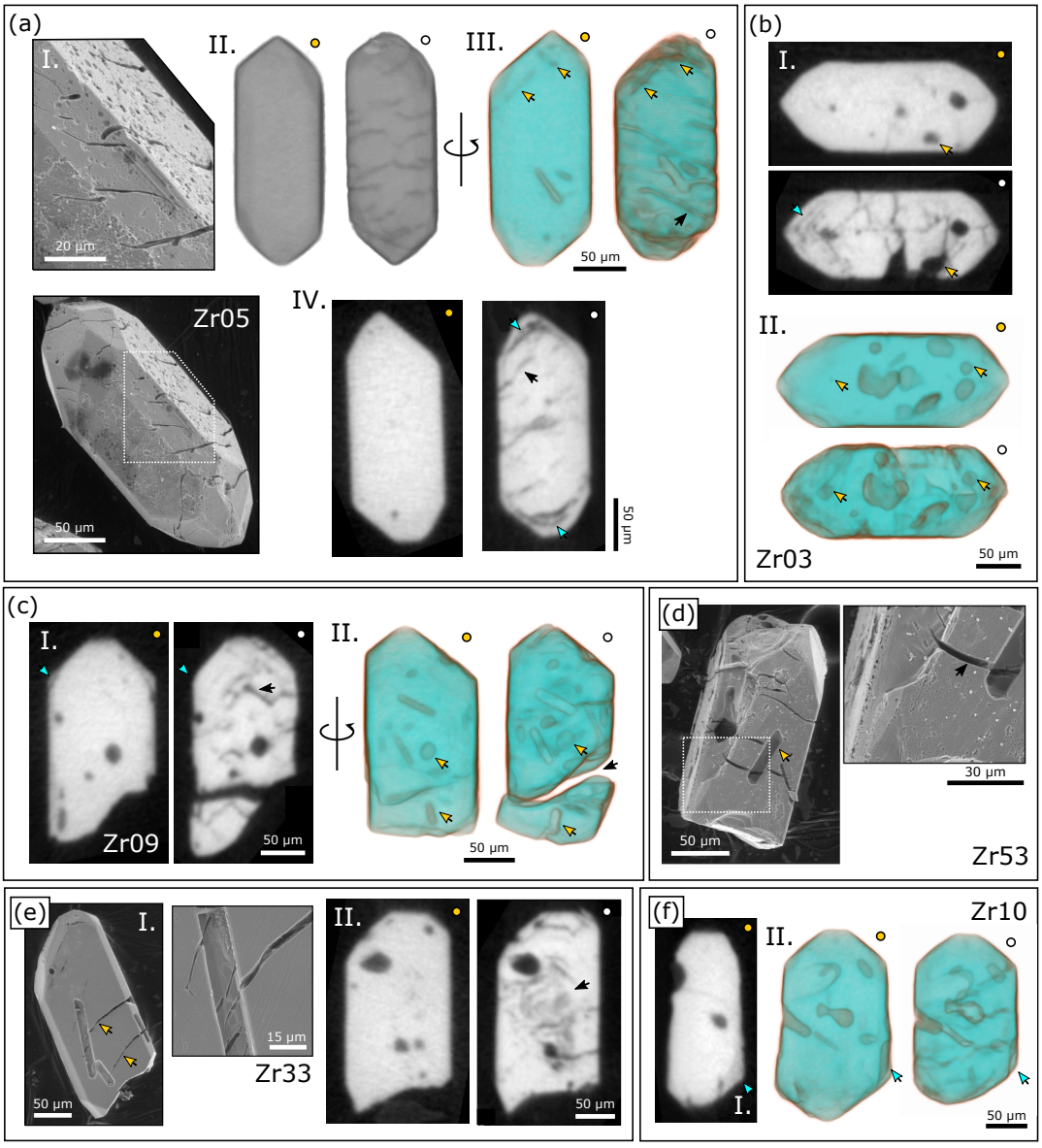

Before(●) and after(○) partial dissolution

rapidly occur (Holland and Gottfried, 1955; Murakami et al., 1991; Ewing et al., 2003; Nasdala et al., 2004). Like AS3, we find that low density rims and interior zones are removed by chemical abrasion at low leaching temperatures and duration (180 °C, 4 h).

SE images of SAM-47 residues treated at 180 °C for 4 h show a range in surface textures (Fig. 12). Some grains have smooth, unetched surfaces while others are more strongly etched. These variations likely reflecting inter-crystalline variations in radiation

https://doi.org/10.5194/gchron-2022-19
Preprint. Discussion started: 26 July 2022

Figure 12: SE and μCT images of SAM-47 grains pre- and post-chemical abrasion at 180 °C for 4 h. **(a)** I. SE images of Zr05 showing deep grooves on the grain's surface and a sponge-like etch texture. II. Opaque 3D rendering of μCT data showing that these surface fractures are only apparent after partial dissolution. III. Semi-transparent 3D rendering of μCT data with yellow arrows marking inclusions removed by partial dissolution. IV. 2D μCT image slices highlighting an example of an acid path into the grain interior (black arrow) and the removal of oscillatory compositional zones (teal arrow). **(b)** I. 2D μCT image slices showing the removal of fine-scale oscillatory compositional zones (teal arrow) and a mineral inclusion (yellow arrows) in Zr03. II. Semi-transparent 3D rendering of μCT data with yellow arrows depicting the removal of more mineral inclusions. **(c)** I. 2D μCT image slices of Zr09 showing the removal of a low-density rim (teal arrow) and an acid path into the grain interior (black arrow). II. Semi-transparent 3D rendering of μCT data highlighting the removal of inclusions (yellow arrows) and the formation of a large fracture (black arrow). **(d)** SE images of Zr53 showing crystal-shaped voids interpreted as dissolved surface-reaching inclusions (yellow arrow) and the fractures that crosscut these voids (black arrow). **(e)** SE images of Zr33 again showing fractures cross-cutting inclusions removed by partial dissolution (yellow arrows) and a smooth grain surface. II. 2D μCT image slices showing a convolute pattern of material dissolved from the crystal core. **(f)** I. 2D μCT image slices highlighting a low-density rim on Zr10. II. Semi-transparent 3D rendering of μCT data showing the removal of this rim.

damage. Large prismatic voids on grain surfaces indicate that low-intensity chemical abrasion removes surface-reaching inclusions. Most prismatic voids are crosscut by large fractures, while other grains have finer sinuous fracture patterns not associated with surface-reaching inclusions. μCT imaging shows that many most zircon residues treated at 180 °C for 4 h have fractures or acid paths to grain interiors that were not visible in the pre-etching image data. These paths have allowed for the dissolution of inclusions, fine-scale oscillatory zones, and convolute zones from crystal interiors.

SE images of SAM-47 residues treated at 210 °C for 4 h have deeper, sponge-like etching textures (Fig. 13). Many grains look dog-chewed. Etch pits are larger with diamond-like shapes similar to those observed in AS3 crystals treated at either 210 °C for 4 h or 180 °C for 12 h, and fractures are commonly wider. SE images again show the removal of surface-reaching inclusions, and the shell-like appearance of some residues hints at the removal of interior zones. μCT images of residues treated at 210 °C for 4 h reveal significant dissolution in grain interiors. Oscillatory compositional zones and inclusions have been removed from deep within crystal cores. Acid paths are in general wider and more interconnected, and fractures crosscut where mineral inclusions once were. We also observe fracture patterns similar to the dumbbells observed in AS3 residues. In a visual game of connect-the-dots in a μCT image slice of Zr30 (Fig. 13a-II), dumbbell-like features appear to crosscut what is likely a continuous, oscillatory compositional zone. Other fractures appear to radiate from the dumbbell features. We see dumbbell-like fracture patterns again in sample Zr36 (Fig. 13b-III) where crosscutting fractures

https://doi.org/10.5194/gchron-2022-19
Preprint. Discussion started: 26 July 2022

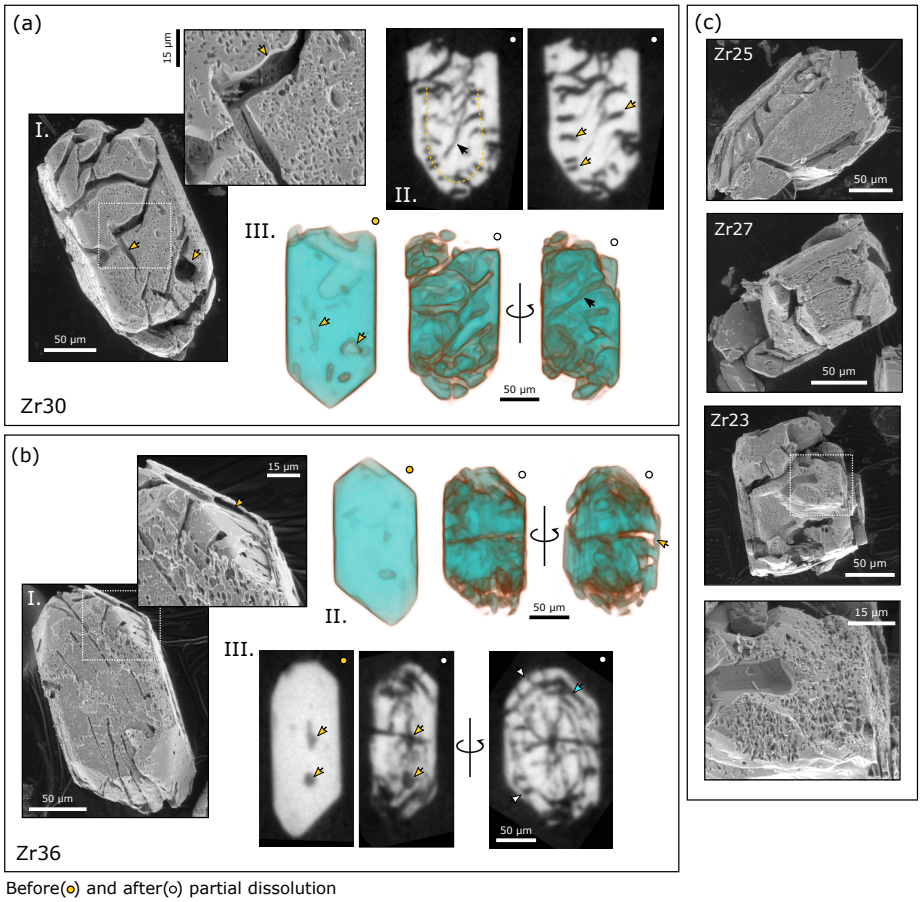

Figure 13: SE and µCT images of SAM-47 grains pre- and post-chemical abrasion at 210 °C for 4 h. **(a)** I. SE images of Zr30 showing wide fractures, the removal of mineral inclusions (yellow arrows), and a moderately etched surface. II. 2D µCT image slices highlighting dumbbell-like features (yellow arrows) interpreted to cross-cut what could be a concentric compositional zone (yellow dashed line). The black arrow exhibits how fractures radiate from the dumbbell features. III. Semi-transparent 3D rendering of µCT data. Yellow arrows correlate to those in I. The black arrow highlights how the fractures observed on the surface propagate through the crystal interior. **(b)** I. SE images of Zr36 showing fractures, diamond-shaped etch pits, and the targeted removal of a compositional zone (yellow arrow). II. Semi-transparent 3D rendering of µCT data. The yellow arrow highlights the grain's shell-like appearance because of significant dissolution in the grain's interior. III. 2D µCT image slices showing the removal of mineral inclusions (yellow arrows), oscillatory zones (teal arrow), and dumbbell-like fractures that appear to cross-cut compositional zones (white arrows). **(c)** SE images of dog-chewed zircon residues Zr25, Zr27, and Zr25.

connect different oscillatory zones removed by dissolution to one another and to the grain surface.

https://doi.org/10.5194/gchron-2022-19
Preprint. Discussion started: 26 July 2022

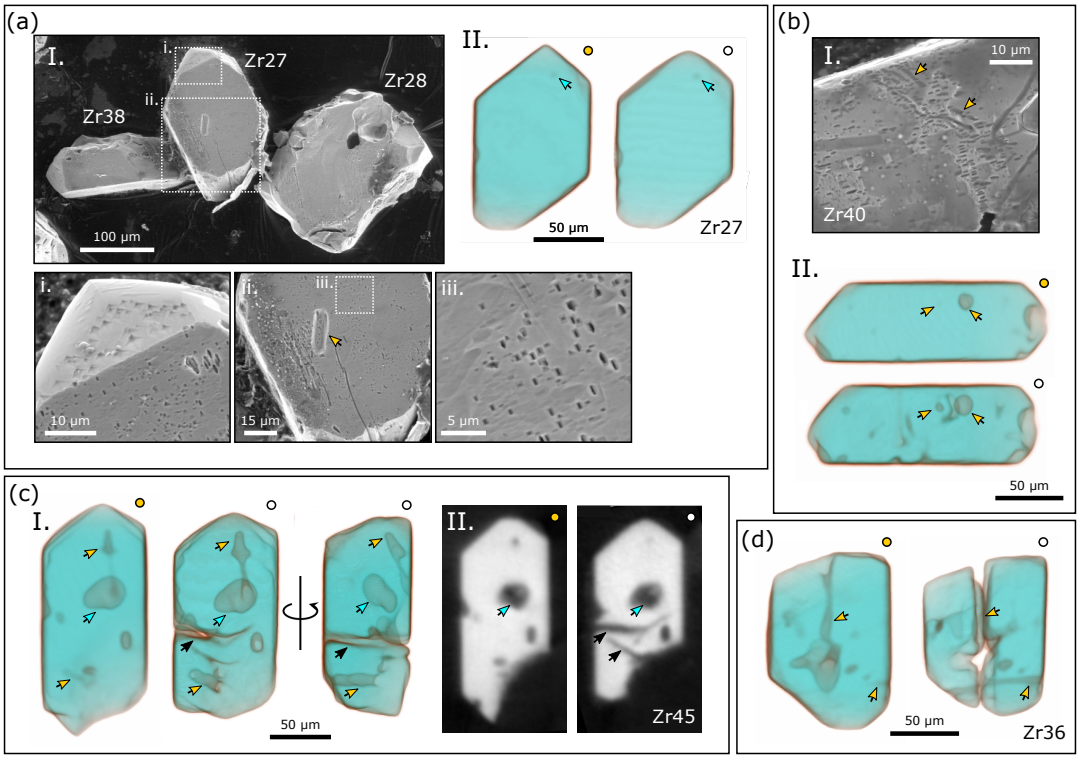

Before(●) and after(○) partial dissolution

Figure 14: SE and µCT images of KR18-04 grains pre- and post-chemical abrasion at 180 °C for 12 h. **(a)** I. A low magnification SE image of zircon samples Zr38, Zr27, and Zr28 and higher magnification images of Zr27 showing close up images of rectangular and triangular etch pits and the removal of a surface-reaching inclusion (yellow arrow). II. Semi-transparent 3D rendering of µCT data for Zr27. Arrows highlight an inclusion inferred to have survived partial dissolution. **(b)** I. SE image of Zr40 with linear etch pit arrays likely indicative of dislocations. II. Semi-transparent 3D rendering of µCT data highlighting inclusions that dissolved. **(c)** I. Semi-transparent 3D rendering of µCT data for Zr45. Teal arrows highlight a large inclusion inferred to have survived partial dissolution, while yellow arrows mark inclusions that dissolved. Black arrows mark acid paths. II. 2D µCT image slices. Teal arrows mark the same multi-phase inclusion in I. Black arrows mark acid paths not apparent in the before imagery dataset. **(d)** Semi-transparent 3D rendering of µCT data for Zr36. Yellow arrows highlight surface-reaching inclusions removed by partial dissolution, resulting in a large cavity in the grain's interior.

3.3.3 KR18-04

Images of annealed and chemically abraded KR18-04 grains treated at 180 °C or 210 °C for 12 h are presented in Fig. 14 and Fig. 15, respectively. SE images of residues treated at 180 °C show intact-grains with mildly etched surfaces (Fig. 14). Etch pits on (100) are small, prismatic, and generally rectangular, while etch pits on other crystal faces are more triangular, highlighting that the shape of etch pits are crystallographically

https://doi.org/10.5194/gchron-2022-19
Preprint. Discussion started: 26 July 2022

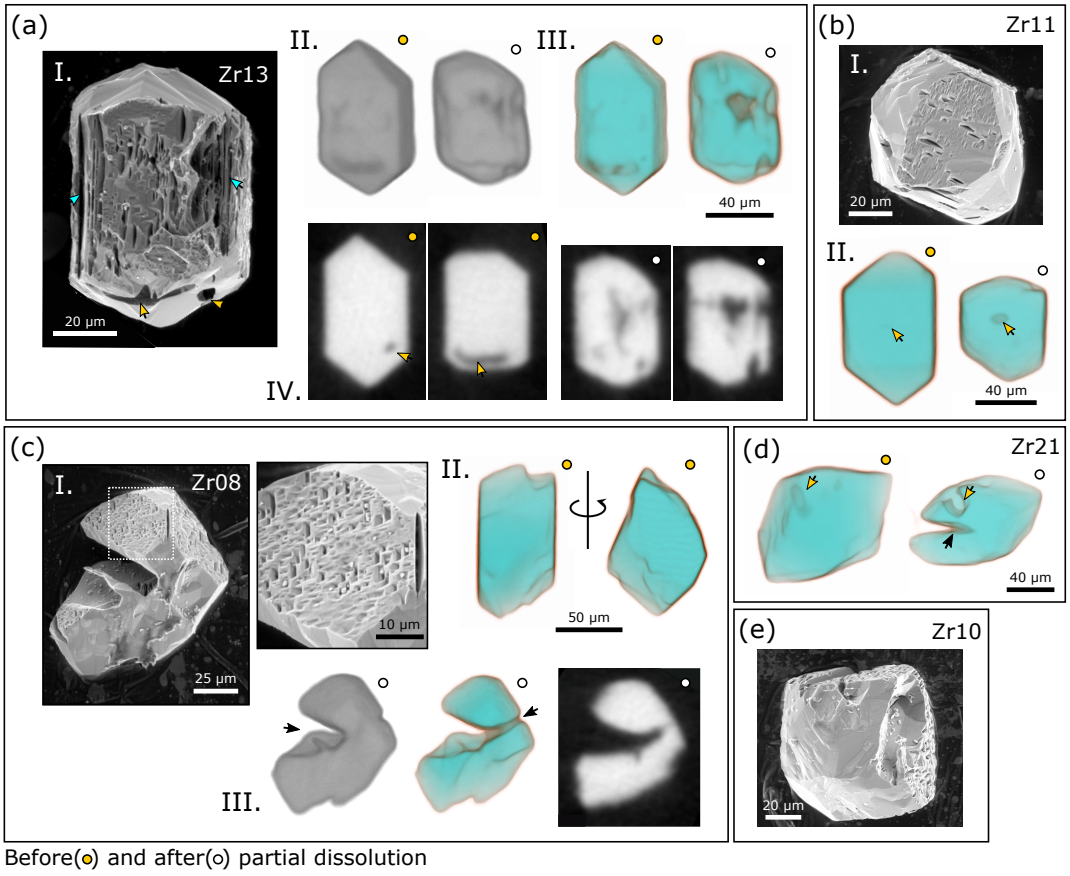

Figure 15: SE and µCT images of KR18-04 grains pre- and post-chemical abrasion at 210 °C for 12 h. **(a)** I. SE image of Zr13 showing dissolved inclusions (yellow arrows) and the removal of oscillatory zones (teal arrows). II. Opaque 3D rendering of µCT data. III. Semi-transparent 3D rendering of µCT data. IV. Representative 2D µCT image slices indicate that a significant amount of zircon material was dissolved from the grain's interior. Yellow arrows correlate to those in I. **(b)** I. SE image of Zr11 showing deep etch pits on (100) with the long axes oriented parallel to the crystal's *c*-axis. Etch pits are absent from other crystal faces. II. Semi-transparent 3D rendering of µCT data showing a dissolved inclusion. **(c)** I. SE images of Zr08. High magnification image shows closely spaced and overlapping prismatic etch pits that form a sponge-like texture. II. Semi-transparent 3D rendering of µCT data acquired before partial dissolution. III. Opaque and Semi-transparent µCT 3D renderings and a representative 2D µCT image slice of the sample after partial dissolution. Black arrows highlight acid paths into the grain interior. **(d)** Semi-transparent 3D rendering of µCT data for Zr21. Yellow arrows mark an inclusion that dissolved. The black arrow highlights the acid path that inexplicably cut into the grain interior. **(e)** SE image of Zr10 with deep prismatic etch pits present on some grain surfaces but not others.

controlled. Linear etch pit arrays suggest the dissolution of defects related to dislocation loops.

https://doi.org/10.5194/gchron-2022-19
Preprint. Discussion started: 26 July 2022

Large crystal-shaped voids on grain surfaces indicate that surface-reaching inclusions are removed by chemical abrasion. μCT images of residues treated at 180 °C indicate that partial dissolution removes some – but not all – mineral inclusions from crystal interiors. For example, the large multi-phase inclusion in Fig. 14c-I is interpreted to have survived partial dissolution since 1) there is apparent change to the grayscale intensities of either phase relative to that of background, 2) there is no apparent change to the inclusion's size or morphology, and 3) there is no evidence that an acid path has reached the inclusion. We note that beam hardening effects make it challenging to identify whether or not smaller inclusions have survived chemical abrasion. In such cases, grayscale intensity values cannot be used to identify whether or not an inclusion has been removed.

We note that some residues have fractures or acid paths that lack obvious precursors in the before imagery dataset. Qualitatively, before-and-after μCT imagery suggest minimal volume loss and a slight shortening of prismatic grain's c-to-a aspect ratio.

SE images of residues treated at 210 °C show the removal of fine-scale oscillatory zones and surface-reaching inclusions. Etch pits are well-preserved on some crystal faces including (100) and entirely absent on others. Etch pits are generally larger than those observed in 180 °C residues. Many are deep, rectangular, and well-faceted. The long axes of deep rectangular pits align parallel to the crystallographic *c*-axis, while the long axes of shallower rectangular pits align parallel to the *a*-axis. Etch pit clusters have a sponge-like texture. μCT images of residues treated at 210 °C show that inclusions and zircon material have been dissolved from grain interiors. Some grains have deep carveouts from crystal interiors with no obvious structural precursor in the before imagery dataset. Before-and-after imagery suggest higher volume loss and a pronounced shortening of some grains' aspect ratio.

3.3.4 BOM2A

Images of annealed and chemically abraded BOM2A grains treated at 180 °C or 210 °C for 12 h are presented in Fig. 16 and Fig. 17, respectively. SE images of residues treated at 180 °C are largely intact (Fig. 16). Similar to KR18-04 residues leached under the same conditions, etch pits are small and rectangular. Some etch pits are isolated while others are interconnected. Some surfaces have deep voids that penetrate the grain interior but do not correlate with inclusions. μCT images qualitatively suggest minor volume loss with a slight shortening along a crystal's c-axis. Chemical abrasion appears to dissolve surface-reaching inclusions and some – but not all – inclusions from crystal interiors. Some residues have fractures that are spatially associated with inclusions.

https://doi.org/10.5194/gchron-2022-19
Preprint. Discussion started: 26 July 2022

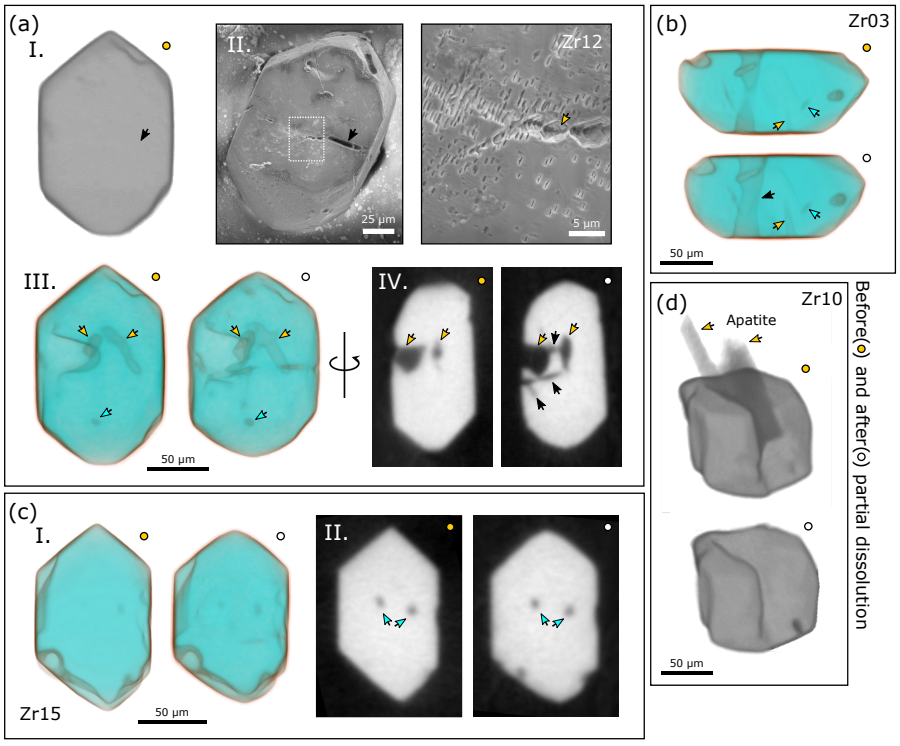

Figure 16. SE and µCT images of BOM2A grains pre- and post-chemical abrasion at 180 °C for 12 h. **(a)** I. Opaque 3D rendering of µCT data for Zr12. II. SE image of grain surface with close up image of clustered and isolated rectangular etch pits. The black arrow points to a void in the crystal perhaps related to a surficial inclusion not apparent in the pre-chemical abrasion dataset, and the yellow arrow highlights another interesting dissolution feature. III. Semi-transparent 3D rendering of µCT data showing inclusions removed by partial dissolution (yellow arrows) and inclusions inferred to have survived (teal arrows). IV. 2D µCT image slices with yellow arrows depicting inclusions dissolved during chemical abrasion and black arrows highlighting acid paths. **(b)** Semi-transparent 3D rendering of µCT data for Zr03 showing inclusions removed by partial dissolution (yellow arrows) and inclusions inferred to have survived (teal arrows). The black arrow highlights an acid path cutting through the crystal interior. **(c)** I. Semi-transparent 3D rendering of µCT data for Zr15 suggesting a slight shortening along the *c*-axis. II. 2D µCT image slices showing inclusions inferred to have survived partial dissolution. **(d)** Opaque 3D rendering of µCT data for Zr10 showing the removal of large, protruding apatite inclusions by partial dissolution.

SE images of residues treated at 210 °C show etch pits are preserved on some crystal faces but not others suggesting a crystallographic control on etch pit formation or preservation (Fig. 16). Like KR18-04 residues leached under the same conditions, etch pits are larger with well-developed facets. Some are isolated will others interconnect to form acid paths into grain interiors. The long axes of deep, octahedral etch pits on (100) align with the crystal's *c*-axis, while the long axes of shallower etch pits that form perpendicular to the octahedral ones align with the crystal's *a*-axis. Some SE images

https://doi.org/10.5194/gchron-2022-19
Preprint. Discussion started: 26 July 2022

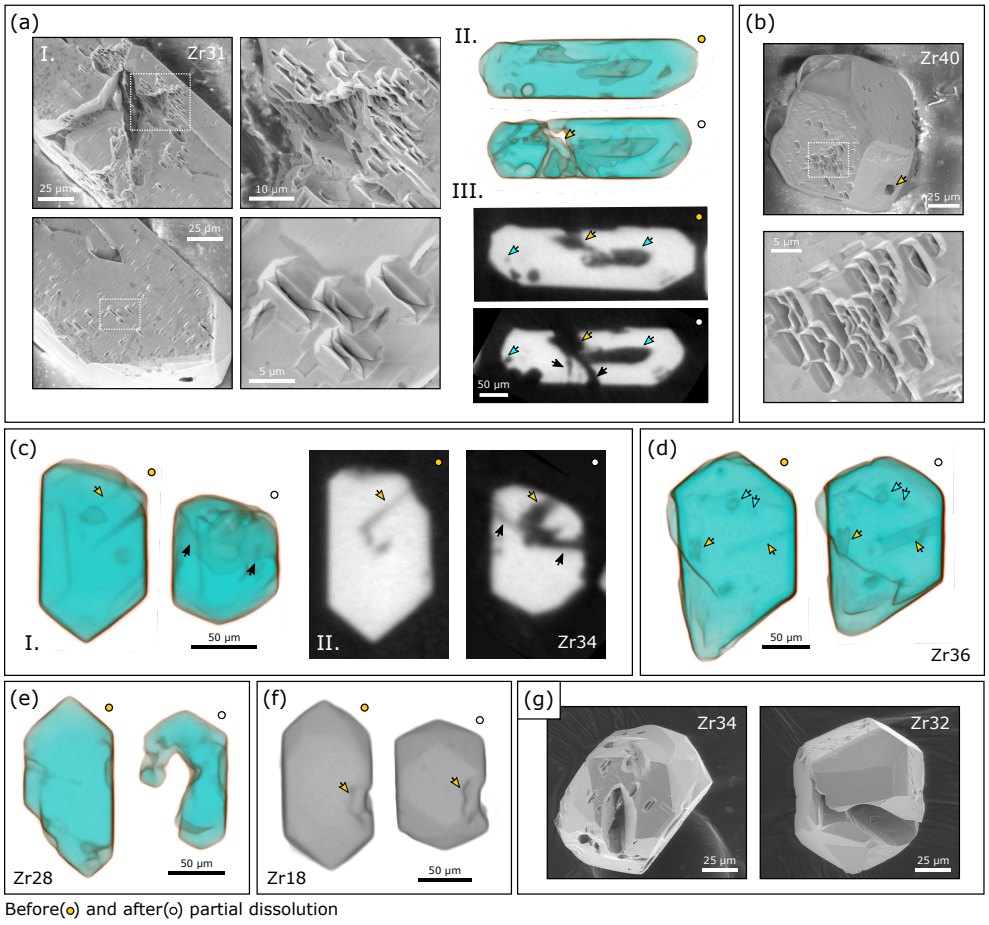

Figure 17: SE and µCT images of BOM2A grains pre- and post-chemical abrasion at 210 °C for 12 h. **(a)** I. SE images of Zr31 showing deep fractures penetrating the grain's interior. Close up images show well-faceted etch pits on (100) some of which are isolated whiles others are interconnected. The long axes of deep, octahedral etch pits are oriented parallel to the *c*-axis, whereas the long axes of shallower etch pits are oriented parallel to the *a*-axis. II. Semi-transparent 3D rendering of µCT data again highlighting the development of large fractures. III. 2D µCT image slices. Teal arrows highlight inclusions that were dissolved, the yellow arrow points to a surface-reaching inclusion that acted as an acid path into the grain interior, and the black arrow highlights acid paths not observed in the before imagery dataset. **(b)** SE images of Zr40 that demonstrates how some crystallographic faces are strongly etched while others are pristine. Etch pits are again strongly prismatic and sometimes interconnected. The yellow arrow points to a void where there once was an inclusion. **(c)** I. Semi-transparent 3D rendering of µCT data for Zr34 showing a significant shortening of the crystal's *c*-axis. II. 2D µCT image slices. The yellow arrows highlight surface-reaching inclusions removed by partial dissolution. Black arrows mark acid paths not apparent in the before imagery dataset. **(d)** Semi-transparent 3D rendering of µCT data for Zr36. Teal arrows highlight inclusions inferred to have survived partial dissolution. Yellow arrows highlight inclusions that were dissolved. **(e)** Semi-transparent 3D rendering of µCT data for Zr28 showing significant volume loss from the grain interior. **(f)** Opaque 3D rendering of µCT data for Zr18. Yellow arrows highlight how some topographic features are preserved during partial dissolution despite significant volume loss. Note how crystal facets are better developed after partial dissolution. **(g)** Low magnification SE images of Zr34 and Zr32 showcasing the crystallographic-dependence of surface etching and acid paths that cut deep into grain interiors.

show that acid has penetrated deeply into grain interiors forming what look like

https://doi.org/10.5194/gchron-2022-19
Preprint. Discussion started: 26 July 2022

caverns. Many of these caverns lack precursors in pre-etching images. μCT images show that the dissolution of surface-reaching inclusions commonly allows acid into crystal cores. We find that some of the fractures observed in SE images are spatially associated with large mineral inclusions. Like the 180 °C leach, we find that leaching at 210 °C removes some – but not all – interior inclusions. Qualitatively, volume loss appears greater at 210 °C, and the *c*-axis is considerably shorter in most crystals after partial dissolution. Before-and-after images show that some topographic features are preserved during chemical abrasion. We also find that some residues are more strongly faceted than they were prior to chemical abrasion.

3.4 Quantifying volume loss and changes to crystal morphology

All quantitative measurements made using the ruler and segmentation functions in Dragonfly ORS software for samples KR18-04 and BOM2A are presented in supplementary Tables S2 and S3 and summarized in Fig. 18. We find that leaching at 180 °C for 12 h causes a ~5 to 10 % decrease in the length of a crystal's *c*-axis (Fig. 18a). Increasing the leaching temperature to 210 °C results in a greater degree of shortening on the order of ~15 to 30 %. In contrast, the length of a crystal's *a*-axes shows little (maximum <4 %) to no change after leaching at 180 °C or 210 °C (Fig. 18b). Consequently, the aspect ratio (c/a) of a crystal decreases during chemical abrasion (Fig. 18c). Note, a 2 % change in a crystal with an initial axis length of 80 μm equates to a change of 1.6 μm which is approximately the spatial resolution of our μCT dataset (1.62 μm). As such we take ~2 % to be a minimum estimate for our measurement error.

Estimated volume losses are presented in Fig. 18d. Our SE images clearly indicate that the spatial resolution of our μCT dataset does not adequately capture fine-scale dissolution features. As such, we consider our volume estimates based on grayscale segmentation to reflect first-order approximations for minimum volume loss. We find that chemical abrasion at 180 °C for 12 h dissolves ~5 to 10 % of a grain by volume, whereas chemical abrasion at 210 °C for 12 h dissolves ~25 to 50 % of a grain by volume. Although there is considerable overlap between the BOM2A and KR18-04 datasets at both leaching conditions, KR18-04 values are skewed toward a greater degree of volume loss than BOM2A. This is likely due to the impact of radiation damage on zircon solubility; unannealed KR18-04 grains on average have higher initial alpha doses than unannealed BOM2A grains.

Fig. 18e suggests that there may be a weak correlation in which crystals with aspect ratio's <2.5 dissolve more readily than crystals with aspect ratio >2.5 amongst samples leached at 210 °C. This reflects the fact that crystals with lower aspect ratios have a higher proportion of faster dissolving surfaces. The fact that this correlation is so weak,

https://doi.org/10.5194/gchron-2022-19
Preprint. Discussion started: 26 July 2022

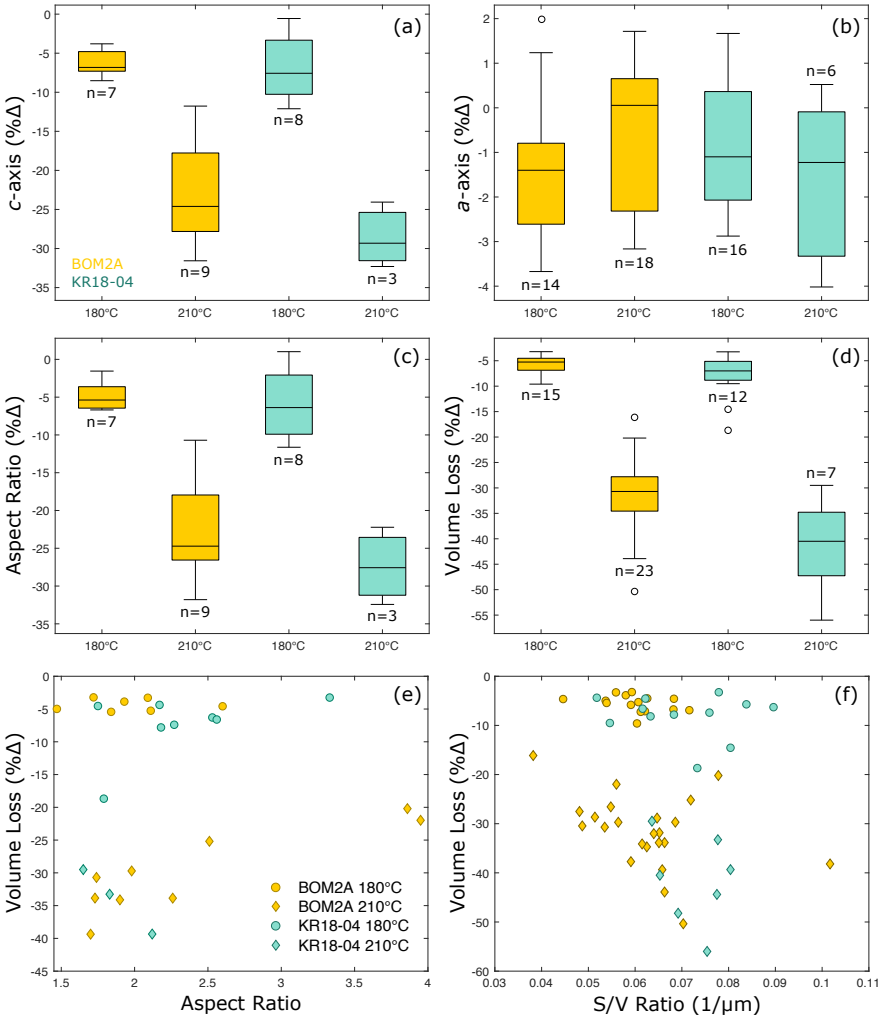

Figure 18: Data plots summarizing crystal morphology, volume, and surface area measurements for KR18-04 and BOM2A. **(a)** Boxplot showing how the length of a grain's *c*-axis changes during chemical abrasion. In all box plots, the central line represents the dataset's median, the box extends to the dataset's 25th and 75th percentiles, the whiskers extend to include the full data range excluding outliers, and circles markers are outliers that exceed the 99% confidence interval. **(b)** Boxplot showing how the length of a grain's *a*-axis changes during chemical abrasion. **(c)** Boxplot showing how a grain's aspect ratio (*c*/*a*) changes during chemical abrasion**. (d)** Boxplot showing estimated volume loss during chemical abrasion. **(e)** Scatter plot showing the relationship between a grain's initial aspect ratio and estimated volume loss. **(f)** Scatter plot showing the relationship between a grain's initial surface-to-volume ratio and estimated volume loss.

527

https://doi.org/10.5194/gchron-2022-19
Preprint. Discussion started: 26 July 2022

however, likely indicates that a crystal's bulk radiation damage has a greater control on dissolution than its aspect ratio. The data in this figure, however, clearly stresses that leaching temperature ultimately has more control than aspect ratio on the rate of zircon dissolution. There is also not a clear correlation between a grain's initial surface area-to-volume ratio and volume loss (Fig 18f).

4 Discussion

4.1 The Mechanics of Zircon Dissolution

4.1.1 Higher damage grains

Except for low-density metamict rims that are removed by low-intensity chemical abrasion (180 °C for 4 h), we find that AS3 and SAM-47 samples – which have initial alpha doses between ~2×10^{17} α/g to >1×10^{19} α/g – do not predominantly dissolve from rim-to-core. Instead, our results suggest that acid often reaches and dissolves material from grain interiors including inclusions and soluble oscillatory compositional zones with higher degrees of radiation damage (Fig. 9 – Fig. 13) leaving behind a more crystalline zircon residue free of inclusions (Fig. 5).

In higher damage grains, fractures play a fundamental role in zircon dissolution by providing acid access to crystal interiors. While fractures are common in CL and BSE images of annealed AS3 and SAM-47 grains, fractures are rare in μCT images of annealed grains. We attribute the apparent discrepancy between our SEM and μCT dataset to the difference in spatial resolution between the two imaging methods. Fractures are likely visible in μCT zircon residues because dissolution has widened them beyond the dataset's 1.62 μm spatial resolution (Fig. 9b-I).

We find that many fractures observed in SE and μCT images of zircon residues are spatially associated with radiation damage zoning (Fig. 10a, Fig. 11a-b, and Fig. 13b). Radial or concentric fracturing related to internal stresses caused by volume expansion of radiation-damaged domains is a common feature in zircon (Chakoumakos et al., 1987; Lee and Tromp, 1995). Fracturing has also been attributed to internal stresses caused by volume reduction due to radiation damage annealing (Geisler et al. 2001a, Geisler et al. 2002). CL images of annealed AS3 samples demonstrate that fractures associated with radiation damage zoning are often present prior to partial dissolution in HF acid (Fig. 3a-I, a-II, and a-III). Some of the fractures observed in CL images of AS3 grains show evidence of hydrothermal alteration indicating that they are geological in nature (Fig. 3a-I). We consider it likely, however, that some fractures developed during dry annealing at 900 °C for 48 h or perhaps even during hydrothermal annealing in HF

https://doi.org/10.5194/gchron-2022-19
Preprint. Discussion started: 26 July 2022

(Geisler et al., 2001b; Geisler et al., 2002). Dual radiation damage accumulation and annealing, fracturing mechanisms best explain why some fractures in zircon residues crosscut zones of relatively high radiation damage while others crosscut zones of relatively low radiation damage (Fig. 10a). Radiation damage zoning fracturing mechanisms also explain why complex fracture networks tend to develop within certain compositional zones (Fig. 10a, Fig. 11a).

Fractures are also commonly associated with inclusions. We observe radial fractures around melt inclusions in μCT images of AS3 residues (Fig. 9a-b) and fractures that crosscut mineral inclusions in SE and μCT images of SAM-47 residues (Fig. 12d-e). Similar fractures are also observed in BSE images of annealed SAM-47 grains (Fig. 3b). BSE images of unannealed SAM-47 grains confirm that some of these fractures formed prior to the start of the experiment. We hypothesize, however, that some fractures likely developed during laboratory annealing at 900 °C for 48 h, since zircon and inclusions have different material properties such as coefficients of thermal expansion (e.g., Subbarao et al., 1990; Hovis et al., 2015). Stress fractures around inclusions have long been used to identify heat treatment in gemstones (Crowningshield and Nassau, 1981; Nassau 1981).

While fractures related to radiation damage zoning and inclusions are the major highways providing acid access to crystal interiors, SE images of overlapping etch pits indicate that acid also percolates across regions with high defect densities including zones of higher radiation damage (Fig. 10a, Fig. 11) and regions with dislocation loops (Fig. 10a-iii). Increasing the temperature or duration of acid leaching results in more pronounced and interconnected etching textures on grain surfaces, wider acid paths, and the formation of more complex dissolution networks deep within crystal interiors.

4.1.2 Lower damage grains

The mechanics of zircon dissolution are considerably different for samples KR18-04 and BOM2A. Initial alpha dose estimates for these samples range from ~6×10^{15} to 7×10^{17} α/g (Fig. 6). Fractures spatially associated with large mineral inclusions in μCT images of chemically abraded residues still play an important role as acid conduits to grain interiors (Fig. 14d, Fig. 16a, Fig. 17a). We again interpret such fractures to most likely form during laboratory annealing at 900 °C for 48 h due to internal stresses caused by differences in coefficients of thermal expansion (Crowningshield and Nassau, 1981; Nassau, 1981; Subbarao et al., 1990; Hovis et al., 2015). Fracturing related to radiation damage zoning, however, does not appear to contribute to zircon dissolution in samples with less radiation damage and more muted intracrystalline variations. In

https://doi.org/10.5194/gchron-2022-19
Preprint. Discussion started: 26 July 2022

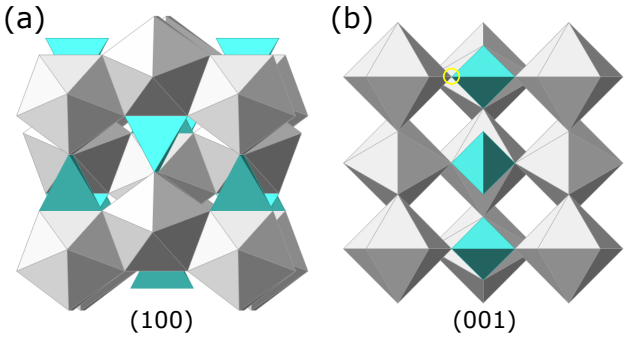

Figure 19: Projections of the zircon crystal structure (Hazen and Finger, 1979; Finch and Hanchar, 2003). ZrO_8 polyhedra are in light gray and SiO_4 tetrahedra are in teal. **(a)** Projection on (100) looking down the *a*-axis. The *c*-axis is vertical to the page, and the a_2-axis is horizontal. **(b)** Projection on (001) looking down the *c*-axis. The yellow circle highlights the corner-sharing bonds between the SiO_4 tetrahedra and the ZrO_8 polyhedra. Projections were rendered using CrystalMaker® software.

some samples though, results suggest that chemical abrasion does dissolve some soluble concentric zones from crystal interiors (Fig. 15a).

Other mechanisms by which acid reaches a grain interior's is via the dissolution of surface reaching inclusions (Fig. 14d, 15a, 16d) and the percolation of acid across regions with higher defect densities and overlapping etch pits (Fig. 15, Fig. 16a, Fig. 17a-b). In some samples, chemical abrasion dissolves large volumes from crystal cores without clear structural reasons (Fig. 15c-d, Fig. 17e). This could reflect the dissolution of zones with more radiation damage, but the pattern of material dissolved does not obviously conform with the growth zonation patterns expected for these samples. Combined, these various acid paths lead to the dissolution of some – but not all – interior inclusions.

Importantly, μCT measurements indicate that dissolution in highly crystalline material is crystallographically-controlled and strongly anisotropic. Most dissolution occurs along the *c*-axis. Etch pits preserved on (100) suggest that dissolution along the *a*-axis is mostly limited to the dissolution of defects that intersect the grain surface. In the (100) and (010) projections of the zircon structure ZrO_8 polyhedra share edges with adjacent ZrO_8 polyhedra and SiO_4 tetrahedra (Fig. 20) (Hazen and Finger, 1979; Finch and Hanchar, 2003). Whereas in the (001) projection of the zircon structure, ZrO_8 polyhedra share edges with adjacent ZrO_8 polyhedra and *corners* with adjacent SiO_4 tetrahedra. Based on our findings, we infer that these corner sharing bonds in the (001) plane are easier to break during dissolution than the solely edge-sharing bonds in the (100) and (010) planes causing faster dissolution along the *c*-axis. Increasing the leaching

https://doi.org/10.5194/gchron-2022-19
Preprint. Discussion started: 26 July 2022

temperature from 180 °C to 210 °C leads a more significant shortening of a crystal's aspect ratio and greater volume loss. In the absence of acid pathways into crystal interiors, grains with low radiation damage predominantly dissolve from rim-to-core along the crystal's *c*-axis (Fig. 14a, Fig. 15b, and Fig. 16c).

Leaching temperature has the strongest control over volume loss in the two samples analyzed. The slight differences between the BOM2A and KR18-04 minimum volume loss estimates suggest that a crystal's bulk radiation damage also plays an important role. Crystal morphology plays a lesser role in that crystals with very high aspect ratios dissolve more slowly than more equant grains. A grain's initial surface-to-volume ratio appears to have no measurable effect on volume loss.

4.2 Implications for ID-TIMS U-Pb geochronology

4.2.1 Zircon U-Pb ages

The purpose of chemical abrasion is to remove soluble, radiation-damaged domains prior to U-Pb isotopic analysis to mitigate the negative effects of Pb loss on geochronological outcomes (Mattinson et al., 2005; 2011). Recent studies have assessed how different annealing temperatures and partial dissolution conditions affect the U-Pb isotopic and trace elemental composition of zircon residues (Huyskens et al., 2016; Widmann et al., 2019). The goal of this study is to construct a mechanistic understanding of zircon dissolution and identify possible implications for U-Pb dating upon which future geochronological and geochemical investigations – such as the single-crystal stepwise partial dissolution experiments that are currently underway by authors AJM and BS – can build.

Magmatic crystallization of zircon occurs over a period of time within a magma chamber. As such, zircon cores are intrinsically older than zircon rims. A rim-to-core model for zircon dissolution implicitly suggests that dissolving more zircon during chemical abrasion by either increasing the temperature or duration of leaching will remove a greater portion of a crystal's rim and bias its U-Pb date toward an older value. This is especially concerning for geochronological studies of volcanic rocks where the youngest U-Pb date or population of dates is often taken to represent the age of a volcanic eruption.

Our results suggest that most zircon crystals with intermediate-to-high levels of radiation damage do not predominantly dissolve from rim-to-core. While increasing the intensity of chemical abrasion leads to textures indicative of greater volume loss, much of that added loss is from the dissolution of interior zones as opposed to the progressive

https://doi.org/10.5194/gchron-2022-19
Preprint. Discussion started: 26 July 2022

dissolution of crystal rims. Consequently, a typical U-Pb analysis of a zircon residue is more likely to reflect the dissolution of soluble high U zones irrespective of age variation within single grains. In addition to high U zones, inclusions and zircon material surrounding fractures are also dissolved. As such, U-Pb analyses of zircon residues with initial intermediate-to-high radiation damage are more likely to broadly reflect mixed core-rim ages.

Some lower damage grains do predominantly dissolve from rim-to-core along a crystal's *c*-axis. This is most apparent in samples leached at 210 °C for 12 h. Growth zones along *c* are often broader than growth zones along *a*, so a volumetrically greater portion of younger domains are likely removed due to *c*-preferential dissolution; however, since rim material on (100) is preserved due to limited dissolution along *a*, there remains a mixed core-rim age component. Further, our analysis suggests that zircon material is commonly dissolved from crystal interiors in lower damage grains. As such, whether hot leaching causes residue ages to be biased toward older values is likely to depend on crystal-dependent factors such as the number, size, and distribution of mineral inclusions, the distribution of higher U domains, and pre-existing fractures.

In regard to lower damage grains, another point to consider is that our Raman results for chemically abraded zircon residues suggest that small differences in initial alpha doses in low damage grains do not appear to dramatically affect which portions of a grain dissolve. This observation evokes an important question – why does chemical abrasion work to mitigate Pb loss in young, lower damage samples? Perhaps the even more fundamental question is – why does Pb loss occur in highly crystalline grains? Further work is needed to address these outstanding questions.

In most samples regardless of initial damage content, we find that chemical abrasion at 210 °C is more effective at mining out soluble zones from crystal interiors. Based on our mechanistic blueprint, we predict that hotter leaching temperatures are thus more likely to better mitigate Pb-loss in geochronological datasets. An important caveat, however, is that hot leaching may not be appropriate for all samples. Our μCT volume estimates indicate that even in low-to-intermediate damage grains 12 h of partial dissolution at 210 °C can dissolve ~25 to 50% of a grain. This means a substantial portion of radiogenic Pb is lost prior to U-Pb isotopic analysis of the zircon residue lowering the precision of the analysis. This is potentially problematic for young or low-U samples. Even greater volume losses are expected for higher damage grains. More U-Pb isotopic investigations of different chemical abrasion protocols – such as single-crystal stepwise partial dissolution experiments – are needed to find the correct balance between removing domains affected by Pb-loss while preserving enough closed-system material for high-precision geochronological analysis.

https://doi.org/10.5194/gchron-2022-19
Preprint. Discussion started: 26 July 2022

On a secondary note, our study shows that in addition to radiation damage other intrinsic defects such as dislocations are also preferentially dissolved by chemical abrasion. Atom probe studies have shown that dislocation loops can sequester radiogenic Pb and other incompatible trace elements redistributed during shock, metamorphism, or deformation (Reddy et al. 2016, Peterman et al. 2016; 2019). Removing sequestered radiogenic Pb from dislocations by HF leaching should in theory increase U-Pb discordance. However, as radiation damaged domains affected by Pb loss are also dissolved during one-step chemical abrasion, leaching likely leads to a net decrease in U-Pb discordance of the dated residue. Early efforts at stepwise chemical abrasion, however, do suggest that partial dissolution can leach some radiogenic Pb from undigested zircon residues in in unannealed grains – perhaps from dislocations – leading to unwanted U and Pb elemental and Pb isotopic fractionation in early leaching steps (Davis and Krogh, 2000; Mattinson, 2005).

4.2.2 Inclusions and zircon trace element analyses

Integrating chemical abrasion ID-TIMS U-Pb dates with trace element analyses (TEA) of the same volume of dissolved zircon can provide important information about petrogenetic processes (Schoene et al. 2010b). Incompatible trace elements such as common Pb, LREEs, Fe, Al, Ca, and Mn can be introduced during metamictization or hydrothermal alteration (Geisler et al., 2001b; Takehara et al., 2018). Our data suggest that damaged zones are readily dissolved during chemical abrasion, and thus should not affect TEA of zircon residues. The integrative TEA approach, however, broadly assumes that inclusions are also dissolved during chemical abrasion, such that the final volume analyzed is zircon as opposed to a zircon-inclusion mixture. A zircon-inclusion mixture would likely result in anomalous trace element concentrations and – if inclusions are Pb-bearing – artificially high common Pb contents which can affect the precision of the U-Pb analysis (Bell et al. 2019). While geochronologists endeavor to select inclusion-free grains, this is not possible for all zircon samples. Further, not all inclusions can be identified optically with a standard binocular picking scope and excluded from consideration.

The fate of inclusions during chemical abrasion has never been rigorously investigated. Our data suggest that inclusions are readily dissolved in grains with intermediate-to-high radiation damage densities due to the development of stress fractures that form presumably during laboratory annealing at 900 °C. These findings strongly emphasize that the annealing step of chemical abrasion is important not just for minimizing leaching-induced elemental and isotopic fractionation (Mattinson, 2005; 2011), but also for building acid paths into grain interiors for to dissolve inclusions. In lower damage

https://doi.org/10.5194/gchron-2022-19
Preprint. Discussion started: 26 July 2022

grains, fracturing can remove large inclusions during partial dissolution, but some inclusions – especially small ones armored by highly crystalline zircon – can survive 12 h of chemical abrasion at 210 °C. As such, some lower damage residues may be susceptible to inclusion contamination. Increasing the leaching temperature from 180 °C to 210 ° seems to improve the likelihood that inclusions will be removed, but it does not guarantee it. All surface-reaching inclusions, however, are dissolved at the tested leaching conditions.

4.3 Implications for radiation damage annealing models

Previous annealing studies (Zhang et al., 2000; Geisler et al., 2001a; Ginster et al., 2019; Härtel et al., 2021; Ende et al., 2021) and the Raman analyses presented here demonstrate that heating in air at 900 °C for 48 hours anneals a significant fraction of radiation damage in zircon crystals with intermediate-to-high initial radiation damage. The change in the relationship between the widths of the $v_3(SiO_4)$ and E_g peaks (Fig. 5a and Fig. 6a), however, suggest that annealing or radiation damage is not simply the inverse of damage accumulation – i.e. bounding environments in zircon partially annealed by dry laboratory heating are different than bounding environments in zircon affected only by damage accumulation. Given this observation, we caution that an equivalent $v_3(SiO_4)$ peak width – or derived alpha dose estimate – for an annealed grain and for a grain affected only by damage accumulation is unlikely to reflect equivalent damage states which has important implications for the use of Raman-based annealing models (Ginster et al., 2019).

There is also an apparent change in the relationship between the widths of the $v_3(SiO_4)$ and E_g peak after partial dissolution in HF acid in some samples, and a small number of Raman analyses for chemically abraded residues are more crystalline than their annealed counter parts (Fig. 5b and Fig. 6b). Taken together, we interpret these observations to suggest that some radiation damage is annealed hydrothermally during HF leaching in some samples. This is somewhat surprising given how much hotter the earlier dry-annealing step is compared to the partial dissolution temperature (180 or 210 °C). Nonetheless, Widman and colleagues (2019) report similar findings in their study of chemically abraded Plešovice zircon; some of their chemically abraded zircon residues also had more crystalline Raman signatures than zircon fragments that were dry-annealed only.

Together these studies contribute to a large body of experimental evidence that indicates that radiation damage in zircon partially anneals at low temperatures under hydrothermal conditions on short, laboratory timescales (Rizvanova et al. 2000; Geisler et al. 2001b, 2002, 2003). Annealing as well as other recrystallization reactions in zircon

https://doi.org/10.5194/gchron-2022-19
Preprint. Discussion started: 26 July 2022

are likely catalyzed by hydrogen diffusion and ionic exchange reactions between zircon and other soluble cations (Petit et al. 1989, Geisler et al. 2001b, Takehara et al. 2018). As such, the extent to which radiation damage anneals in wet geological environments – and how deeply wet annealing effects extend into crystal interiors – likely depends on a combination of heating temperature, heating duration, and the composition of hydrothermal fluids (Geisler et al. 2001b, 2002).

The kinetics of dry verses wet annealing clearly differ as evidenced by their discrepant temperature sensitivities and hypothesized mechanistic processes. Given the prevalence of fluids in geological environments, it could be argued that geological annealing of radiation damage in zircon most often occurs under hydrothermal conditions. However, most radiation damage annealing models are based on dry annealing kinetics that may poorly approximate geological conditions (Zhang et al. 2000, Geisler et al. 2001a, Yamada et al. 2007, Ginster et al. 2019, Härtel et al. 2021). Some of these models are embedded in thermal modeling programs and used to interpret time-temperature histories from complex zircon fission track and (U-Th)/He datasets (Guenthner et al. 2013, Guenthner 2021). As such, quantifying zircon radiation damage annealing kinetics under hydrothermal conditions could help to improve interpretations of deep-time low-temperature thermochronology datasets. Wet annealing studies would likely also advance our understanding of how Pb is lost from the zircon crystal structure in geological environments. This knowledge could potentially be used to tailor chemical abrasion protocols to improve U-Pb geochronological outcomes for zircon crystals affected by one or more episodes of hydrothermal annealing.

4.4 Imaging radiation damage zoning: Implications for (U-Th)/He thermochronology

The accumulation of radiation damage in zircon has a profound impact on He diffusion kinetics and applications of deep-time zircon (U-Th)/He thermochronology (Guenthner et al. 2013; Cherniak, 2019; Anderson et al. 2017; 2020b). While cathodoluminescence imaging and Raman 2D spectral mapping have previously been used to either qualitatively or quantitatively characterize the distribution of radiation damage in polished zircon grains prior to laser ablation zircon (U-Th)/He analyses (Danišík et al., 2017; Anderson et al., 2017; 2020a), finding a method for rapid and non-destructive 3D characterization of strong radiation damage zoning in unpolished grains for single-crystal zircon (U-Th)/He dating has remained elusive. μCT offers an exciting new way to quickly screen zircon grains for strong radiation damage zoning prior to (U-Th)/He analysis. Strongly zoned grains could either be excluded from datasets or corrections could be applied to account for expected intracrystalline variations in He diffusivity. μCT data can also be used to identify mineral phases or inclusions and intergrowths that might impact He systematics (Cooperdock et al., 2016; Cooperdock and Stockli,

https://doi.org/10.5194/gchron-2022-19
Preprint. Discussion started: 26 July 2022

2018; Cooperdock et al. 2022), and improve alpha ejection corrections by generating more robust surface area-to-volume estimates (Cooperdock et al., 2019) and providing key insights into compositional zoning.

5 Conclusions

Here we present results for a microstructural investigation – X-ray micro-computed tomography (μCT), scanning electron microscopy, and Raman spectroscopy data – of zircon crystals before and after chemical abrasion that yield new insights into the mechanics of zircon dissolution during HF digestion. Selected samples have a range of accumulated alpha doses that cover nearly the full radiation damage spectrum. SE images of chemically abraded zircon residues show that high-U oscillatory zones, radiation damage defects, and other intrinsic defects such as lattice dislocations are preferentially dissolved during acid digestion. In higher damage materials etch pits generally have diamond-like shapes that closely resemble etched fission tracks. At longer leaching durations and in more crystalline zircon samples, etch pit morphology becomes increasingly prismatic due to crystallographically-controlled dissolution. The interconnectivity of etch pits in SE images demonstrates how acid can percolate across regions with high defect densities. Dumbbell features that crosscut radiation damage zones in some SE images highlight the important role that fracturing related to radiation damage accumulation and/or annealing plays in the dissection of higher damage grains. SE images of zircon residues also show that fractures commonly crosscut voids where inclusions once were.

We pair our surface texture catalog with μCT images of the same grains acquired before and after chemical abrasion to understand the effects of HF leaching on crystal cores. We find that the density contrast between crystalline and metamict zircon is apparent in μCT images, making μCT an effective tool for the rapid – and non-destructive – imaging of strong radiation damage zoning in zircon in 3D. We find that most zircon crystals, especially higher damage grains, do not dissolve predominantly from rim-to-core. Low-density rims and interior zones visible in μCT images are dissolved during low intensity chemical abrasion. However, leaching also removes oscillatory zones, material around fractures, and some inclusions from crystal cores. The main mechanisms by which acid reaches grain interiors is via fracturing due to internal stresses caused by radiation damage zoning and inclusions and dissolved surface-reaching inclusions. While many fractures formed geologically, we hypothesize that dry laboratory annealing at 900 °C prior to HF leaching likely contributes to fracture development, making dry annealing a critical step of the chemical abrasion process. Increasing the leaching temperature from 180 °C to 210 °C or increasing the leaching

https://doi.org/10.5194/gchron-2022-19
Preprint. Discussion started: 26 July 2022

duration leads to the development of more extensive dissolution networks in higher damage grains.

More crystalline zircon samples lack fracturing related to radiation damage zoning. Acid still, however, reaches the interior of many crystals via the other acid paths described. Some but not all mineral inclusions are removed after 12 h of chemical abrasion. μCT measurements show that dissolution in lower damage grains is strongly anisotropic. Most dissolution occurs along the crystallographic *c*-axis with minimal dissolution occurring along *a*. Even in lower damage grains, bulk radiation damage appears to be the major factor controlling the degree of volume loss during partial dissolution. Increasing the leaching temperature from 180 °C to 210 °C leads to an up to ~40 % increase in volume loss in the lower-damage grains analyzed.

We broadly discuss potential implications for applications of ID-TIMS U-Pb geochronology. Since most crystals analyzed do not follow a simple rim-to-core dissolution pattern, we expect that most U-Pb analyses of zircon residues reflect mixed core-rim age components. Chemical abrasion at 210 °C appears to more effectively mine out soluble zones from crystal interiors, however increasing the leaching temperature 210 °C also results in higher volume losses that could result in lower-precision U-Pb analyses. More ID-TIMS U-Pb data – such as single crystal step-wise degassing experiments conducted using different leaching conditions – are needed to identify the best balance between removal of damaged material compromised by Pb loss and removal of excess closed-system material. Since some inclusions appear to survive 12 h of chemical abrasion in lower damage samples, trace element analyses of highly crystalline zircon should be evaluated for possible inclusion contamination.

Raman analyses of annealed grains suggest that dry annealing is not the inverse of radiation damage accumulation. Further, Raman data for chemically abraded zircon residues presents additional evidence that some radiation damage anneals hydrothermally at low temperatures (180 °C to 210 °C) which has important implications for the usefulness of current Raman-based dry radiation damage annealing models. We also suggest the μCT imaging could be a useful tool for studying the effects of radiation damage zoning on He diffusion in 3D and for applications of deep-time zircon (U-Th)/He thermochronology.

Supplement. The supplement to this article is available online at:

Author Contributions. AJM designed and conducted the experiments. All authors participated in the interpretation of the experimental results. AJM prepared the figures and manuscript.

https://doi.org/10.5194/gchron-2022-19
Preprint. Discussion started: 26 July 2022

Competing Interests. The authors declare no competing interests.

Acknowledgements. We would like to thank Jessie Maisano of the University of Texas High Resolution CT facility for helping us to acquire μCT data during the height of the global pandemic, and Tom Duffy of Princeton University for use of his Raman system. Thank you also to Mami Takehara of the National Institute of Polar Research in Tokyo, Japan for providing the hydrothermally altered AS3 zircon crystals used in this study. We are indebted to Tyler McKanna for providing computing resources, and we would also like to thank Dawid Szymanowksi for many hours of valuable discussion.

Financial support. This work was supported by research funds provided by the Department of Geosciences at Princeton University granted to Alyssa J. McKanna as part of her Harry Hess Postdoctoral Fellowship.

Review Statement.

References

Anderson, A. J., Hodges, K. V., and van Soest, M. C.: Empirical constraints on the effects of radiation damage on helium diffusion in zircon, Geochim. Cosmochim. Acta, 218, 308–322, https://doi.org/10.1016/j.gca.2017.09.006, 2017.

Anderson, A. J., Hanchar, J. M., Hodges, K. V., and van Soest, M. C.: Mapping radiation damage zoning in zircon using Raman spectroscopy: Implications for zircon chronology, Chem. Geol., 538, 119494, https://doi.org/10.1016/j.chemgeo.2020.119494, 2020a.

Anderson, A. J., van Soest, M. C., Hodges, K. V., and Hanchar, J. M.: Helium diffusion in zircon: Effects of anisotropy and radiation damage revealed by laser depth profiling, Geochim. Cosmochim. Acta, 274, 45–62, https://doi.org/10.1016/j.gca.2020.01.049, 2020b.

Basu, A. R., Chakrabarty, P., Szymanowski, D., Ibañez-Mejia, M., Schoene, B., Ghosh, N., and Georg, R. B.: Widespread silicic and alkaline magmatism synchronous with the Deccan Traps flood basalts, India, Earth Planet. Sci. Lett., 552, 116616, https://doi.org/10.1016/j.epsl.2020.116616, 2020.

Bell, E. A., Boehnke, P., Barboni, M., and Harrison, T. M.: Tracking chemical alteration in magmatic zircon using rare earth element abundances, Chem. Geol., 510, 56–71, https://doi.org/10.1016/j.chemgeo.2019.02.027, 2019.

Bowring, S. A. and Schmitz, M. D.: High-precision U-Pb zircon geochronology and the stratigraphic record, in: Reviews in Mineralogy and Geochemistry Zircon, vol. 53, edited by: Hanchar, J. M. and Hoskin, P. W. O., 305–326, https://doi.org/10.2113/0530305, 2003.

Chakoumakos, B. C., Murakami, T., Lumpkin, G. R., and Ewing, R. C.: Alpha-decay induced fracturing in zircon: The transition from the crystalline to the metamict state, Science, 236, 1556–1559, 1987.

Cherniak, D. J.: Diffusion of helium in radiation-damaged zircon, Chem. Geol., 529, 119308, https://doi.org/10.1016/j.chemgeo.2019.119308, 2019.

Cooperdock, E. H. G. and Stockli, D. F.: Unraveling alteration histories in serpentinites and associated ultramafic rocks with magnetite (U-Th)/He geochronology, Geology, 44, 967–970, https://doi.org/10.1130/g38587.1, 2016.

Cooperdock, E. H. G. and Stockli, D. F.: Dating exhumed peridotite with spinel (U–Th)/He chronometry, Earth Planet. Sci. Lett., 489, 219–227, https://doi.org/10.1016/j.epsl.2018.02.041, 2018.

Cooperdock, E. H. G., Ketcham, R. A., and Stockli, D. F.: Resolving the effects of 2-D versus 3-D grain measurements on apatite (U–Th) / He age data and reproducibility, Gchron., 1, 17–41, https://doi.org/10.5194/gchron-1-17-2019, 2019.

Cooperdock, E. H. G., Hofmann, F., Collins, R. M., Carrera, A., Takase, A., and Celestian, A. J.: Technical note: Rapid phase identification of apatite and zircon grains for geochronology using X-ray micro-computed tomography, GChron., Preprint, https://doi.org/10.5194/gchron-2022-7, 2022.

Crowningshield, R. and Nassau, K.: The Heat and Diffusion Treatment of Natural and Synthetic Sapphires, J. Gemmology, 17, 528–541, https://doi.org/10.15506/jog.1981.17.8.528, 1981.

Danišík, M., McInnes, B. I. A., Kirkland, C. L., McDonald, B. J., Evans, N. J., and Becker, T.: Seeing is believing: Visualization of He distribution in zircon and implications for thermal history reconstruction on single crystals, Sci. Adv., 3, e1601121, https://doi.org/10.1126/sciadv.1601121, 2017.

Davis, D. W. and Krogh, T. E.: Preferential dissolution of ^{234}U and radiogenic Pb from α-recoil-damaged lattice sites in zircon: implications for thermal histories and Pb isotopic fractionation in the near surface environment, Chem. Geol., 172, 41–58, https://doi.org/10.1016/s0009-2541(00)00235-7, 2000.

Davydov, V. I., Crowley, J. L., Schmitz, M. D., and Poletaev, V. I.: High-precision U-Pb zircon age calibration of the global Carboniferous time scale and Milankovitch band cyclicity in the Donets Basin, eastern Ukraine, Geochem. Geophys. Geosyst., 11, n/a-n/a, https://doi.org/10.1029/2009gc002736, 2010.

Ende, M., N., C. C., Reiners, P. W., Zamyatin, D. A., Gain, S. E. M., Wirth, R., and Nasdala, L.: Dry annealing of radiation-damaged zircon: Single-crystal X-ray and Raman spectroscopy study, Lithos, 406, 106523, https://doi.org/10.1016/j.lithos.2021.106523, 2021.

https://doi.org/10.5194/gchron-2022-19
Preprint. Discussion started: 26 July 2022

Ewing, R. C., Meldrum, A., Wang, L., Weber, W. J., and Corrales, L. R.: Radiation effects in zircon, in: Reviews in Mineralogy & Geochemistry, vol. 53, edited by: Hanchar, J. M. and Hoskin, P. W. O., 387–425, https://doi.org/10.2113/0530387, 2003.

Finch, R. J. and Hanchar, J. M.: Structure and chemistry of zircon and zircon-group minerals, in: Reviews in Mineralogy and Geochemistry Zircon, vol. 53, edited by: Hanchar, J. M. and Hoskin, P. W. O., 1–25, https://doi.org/10.2113/0530001, 2003.

Geisler, T., Pidgeon, R. T., Bronswijk, W. van, and Pleysier, R.: Kinetics of thermal recovery and recrystallization of partially metamict zircon: a Raman spectroscopic study, Eur. J. Mineral., 13, 1163–1176, https://doi.org/10.1127/0935-1221/2001/0013-1163, 2001a.

Geisler, T., Ulonska, M., Schleicher, H., Pidgeon, R. T., and Bronswijk, W. van: Leaching and differential recrystallization of metamict zircon under experimental hydrothermal conditions, Contrib. Mineral. Petr., 141, 53–65, https://doi.org/0.1007/s004100000202, 2001b.

Geisler, T., Pidgeon, R. T., Bronswijk, W. van, and Kurtz, R.: Transport of uranium, thorium, and lead in metamict zircon under low-temperature hydrothermal conditions, Chem. Geol., 191, 141–154, https://doi.org/10.1016/s0009-2541(02)00153-5, 2002.

Geisler, T., Trachenko, K., Ríos, S., Dove, M. T., and Salje, E. K. H.: Impact of self-irradiation damage on the aqueous durability of zircon ($ZrSiO_4$): implications for its suitability as a nuclear waste form, J. Phys. Condens. Matter, 15, L597, https://doi.org/10.1088/0953-8984/15/37/l07, 2003.

Ginster, U., Reiners, P. W., Nasdala, L., and N., C. C.: Annealing kinetics of radiation damage in zircon, Geochim. Cosmochim. Acta, 249, 225–246, https://doi.org/10.1016/j.gca.2019.01.033, 2019.

Gleadow, A. J. W., Hurford, A. J., and Quaife, R. D.: Fission track dating of zircon: Improved etching techniques, Earth Planet. Sci. Lett., 33, 273–276, https://doi.org/10.1016/0012-821x(76)90235-1, 1976.

Guenthner, W. R.: Implementation of an alpha damage annealing model for zircon (U-Th)/He Thermochronology with comparison to a zircon fission track annealing model, Geochem. Geophys. Geosyst., 22, https://doi.org/10.1029/2019gc008757, 2021.

Guenthner, W. R., Reiners, P. W., Ketcham, R. A., Nasdala, L., and Giester, G.: Helium diffusion in natural zircon: Radiation damage, anisotropy, and the interpretation of zircon (U-Th)/He thermochronology, Am. J. Sci., 313, 145–198, https://doi.org/10.2475/03.2013.01, 2013.

Härtel, B., Jonckheere, R., Wauschkuhn, B., and Ratschbacher, L.: The closure temperature(s) of zircon Raman dating, GChron., 3, 259–272, https://doi.org/10.5194/gchron-3-259-2021, 2021.

Hazen, R. M. and Finger, L. W.: Crystal structure and compressibility of zircon at high pressure, Am. Mineral., 64, 196–201, 1979.

Holland, H. D. and Gottfried, D.: The effect of nuclear radiation on the structure of zircon, Acta Crystallogr., 8, 291–300, https://doi.org/10.1107/s0365110x55000947, 1955.

Hovis, G., Abraham, T., Hudacek, W., Wildermuth, S., Scott, B., Altomare, C., Medford, A., Conlon, M., Morris, M., Leaman, A., Almer, C., Tomaino, G., and Harlov, D.: Thermal expansion of F-Cl apatite crystalline solutions, Am. Mineral., 100, 1040–1046, https://doi.org/10.2138/am-2015-5176, 2015.

Huyskens, M. H., Zink, S., and Amelin, Y.: Evaluation of temperature-time conditions for the chemical abrasion treatment of single zircons for U–Pb geochronology, Chem. Geol., 438, 25–35, https://doi.org/10.1016/j.chemgeo.2016.05.013, 2016.

Jonckheere, R.: On the densities of etchable fission tracks in a mineral and co-irradiated external detector with reference to fission-track dating of minerals, Chem. Geol., 200, 41–58, https://doi.org/10.1016/s0009-2541(03)00116-5, 2003.

Jonckheere, R. and haute, P. V. den: Observations on the geometry of etched fission tracks in apatite: Implications for models of track revelation, Am. Mineral., 81, 1476–1493, 1996.

Jonckheere, R., Enkelmann, E., and Stübner, K.: Observations on the geometries of etched fission and alpha-recoil tracks with reference to models of track revelation in minerals, Radiat. Meas., 39, 577–583, https://doi.org/10.1016/j.radmeas.2004.08.008, 2005.

Jonckheere, R., Aslanian, C., Wauschkuhn, B., and Ratschbacher, L.: Fission-track etching in apatite: A model and some implications, Am. Mineral., 107, 1190–1200, https://doi.org/10.2138/am-2022-8055, 2022.

Jones, S., Kohn, B., and Gleadow, A.: Etching of fission tracks in monazite: Further evidence from optical and focused ion beam scanning electron microscopy, Am. Mineral., 107, 1065–1073, https://doi.org/10.2138/am-2022-8002, 2022.

Ketcham, R. A., Guenthner, W. R., and Reiners, P. W.: Geometric analysis of radiation damage connectivity in zircon, and its implications for helium diffusion, Am. Mineral., 98, 350–360, https://doi.org/10.2138/am.2013.4249, 2013.

Lee, J. K. W. and Tromp, J.: Self-induced fracture generation in zircon, J. Geophys. Res. Solid Earth, 100, 17753–17770, https://doi.org/10.1029/95jb01682, 1995.

MacLennan, S. A., Eddy, M. P., Merschat, A. J., Mehra, A. K., Crockford, P. W., Maloof, A. C., Southworth, C. S., and Schoene, B.: Geologic evidence for an icehouse Earth before the Sturtian global glaciation, Sci. Adv., 6, eaay6647, https://doi.org/10.1126/sciadv.aay6647, 2020.

Mattinson, J. M.: Zircon U–Pb chemical abrasion ("CA-TIMS") method: Combined annealing and multi-step partial dissolution analysis for improved precision and accuracy of zircon ages, Chem. Geol., 220, 47–66, https://doi.org/10.1016/j.chemgeo.2005.03.011, 2005.

https://doi.org/10.5194/gchron-2022-19
Preprint. Discussion started: 26 July 2022

Mattinson, J. M.: Extending the Krogh legacy: development of the CA-TIMS method for zircon U-Pb geochronology, Can. J. Earth Sci., 48, 95–105, https://doi.org/10.1139/e10-023, 2011.

Meldrum, A., Boatner, L. A., Weber, W. J., and Ewing, R. C.: Radiation damage in zircon and monazite, Geochim. Cosmochim. Acta, 62, 2509–2520, https://doi.org/10.1016/s0016-7037(98)00174-4, 1998.

Meyers, S. R., Siewert, S. E., Singer, B. S., Sageman, B. B., Condon, D. J., Obradovich, J. D., Jicha, B. R., and Sawyer, D. A.: Intercalibration of radioisotopic and astrochronologic time scales for the Cenomanian-Turonian boundary interval, Western Interior Basin, USA, Geology, 40, 7–10, https://doi.org/10.1130/g32261.1, 2012.

Mezger, K. and Krogstad, E. J.: Interpretation of discordant U-Pb zircon ages: An evaluation, J. Metamorph. Geol., 15, 127–140, https://doi.org/10.1111/j.1525-1314.1997.00008.x, 1997.

Mundil, R., Ludwig, K. R., Metcalfe, I., and Renne, P. R.: Age and timing of the Permian mass extinctions: U/Pb dating of closed-system zircons, Science, 305, 1760–1763, https://doi.org/10.1126/science.1101012, 2004.

Murakami, T., Chakoumakos, B. C., Ewing, R. C., Lumpkin, G. R., and Weber, W. J.: Alpha-decay event damage in zircon, Am. Mineral., 76, 1510–1532, 1991.

Nasdala, L., Irmer, G., and Wolf, D.: The degree of metamictization in zircon: a Raman spectroscopic study, Eur. J. Mineral., 7, 471–478, https://doi.org/10.1127/ejm/7/3/0471, 1995.

Nasdala, L., Pidgeon, R. T., Wolf, D., and Irmer, G.: Metamictization and U-Pb isotopic discordance in single zircons: a combined Raman microprobe and SHRIMP ion probe study, Mineral. Petrol., 62, 1–27, https://doi.org/10.1007/bf01173760, 1998.

Nasdala, L., Wenzel, M., Vavra, G., Irmer, G., Wenzel, T., and Kober, B.: Metamictisation of natural zircon: accumulation versus thermal annealing of radioactivity-induced damage, Contrib. Mineral. Petr., 141, 125–144, https://doi.org/10.1007/s004100000235, 2001.

Nasdala, L., Reiners, P. W., Garver, J. I., Kennedy, A. K., Stern, R. A., Balan, E., and Wirth, R.: Incomplete retention of radiation damage in zircon from Sri Lanka, Am. Mineral., 89, 219–231, 2004.

Nassau, K.: Heat treating ruby and sapphire: Technical aspects, Gems Gemol., 17, 121–131, https://doi.org/10.5741/gems.17.3.121, 1981.

Paces, J. B. and Miller, J. D.: Precise U-Pb ages of Duluth Complex and related mafic intrusions, northeastern Minnesota: Geochronological insights to physical, petrogenetic, paleomagnetic, and tectonomagmatic processes associated with the 1.1 Ga Midcontinent Rift System, J. Geophys. Res. Solid Earth, 98, 13997–14013, https://doi.org/10.1029/93jb01159, 1993.

https://doi.org/10.5194/gchron-2022-19
Preprint. Discussion started: 26 July 2022

Palenik, C. S., Nasdala, L., and Ewing, R. C.: Radiation damage in zircon, Am. Mineral., 88, 770–781, https://doi.org/10.2138/am-2003-5-606, 2003.

Peterman, E. M., Reddy, S. M., Saxey, D. W., Snoeyenbos, D. R., Rickard, W. D. A., Fougerouse, D., and Kylander-Clark, A. R. C.: Nanogeochronology of discordant zircon measured by atom probe microscopy of Pb-enriched dislocation loops, Sci. Adv., 2, e1601318, https://doi.org/10.1126/sciadv.1601318, 2016.

Peterman, E. M., Reddy, S. M., Saxey, D. W., Fougerouse, D., Snoeyenbos, D. R., and Rickard, W. D. A.: Nanoscale processes of trace element mobility in metamorphosed zircon, Contrib. Mineral. Petr., 174, 92, https://doi.org/10.1007/s00410-019-1631-1, 2019.

Petit, J.-C., Dran, J.-C., Paccagnella, A., and Mea, G. D.: Structural dependence of crystalline silicate hydration during aqueous dissolution, Earth Planet. Sci. Lett., 93, 292–298, https://doi.org/10.1016/0012-821x(89)90077-0, 1989.

Reddy, S. M., Riessen, A. van, Saxey, D. W., Johnson, T. E., Rickard, W. D. A., Fougerouse, D., Fischer, S., Prosa, T. J., Rice, K. P., Reinhard, D. A., Chen, Y., and Olson, D.: Mechanisms of deformation-induced trace element migration in zircon resolved by atom probe and correlative microscopy, Geochim. Cosmochim. Acta, 195, 158–170, https://doi.org/10.1016/j.gca.2016.09.019, 2016.

Rizvanova, N. G., Levchenkov, O. A., Belous, A. E., Bezmen, N. I., Maslenikov, A. V., Komarov, A. N., Makeev, A. F., and Levskiy, L. K.: Zircon reaction and stability of the U-Pb isotope system during interaction with carbonate fluid: experimental hydrothermal study, Contrib. Mineral. Petr., 139, 101–114, https://doi.org/10.1007/s004100050576, 2000.

Schmitz, M. D. and Davydov, V. I.: Quantitative radiometric and biostratigraphic calibration of the Pennsylvanian–Early Permian (Cisuralian) time scale and pan-Euramerican chronostratigraphic correlation, GSA Bulletin, 124, 549–577, https://doi.org/10.1130/b30385.1, 2012.

Schmitz, M. D., Bowring, S. A., and Ireland, T. R.: Evaluation of Duluth Complex anorthositic series (AS3) zircon as a U-Pb geochronological standard: new high-precision isotope dilution thermal ionization mass spectrometry results, Geochim. Cosmochim. Acta, 67, 3665–3672, https://doi.org/10.1016/s0016-7037(03)00200-x, 2003.

Schoene, B.: Treatise on Geochemistry (Second Edition), in: Treatise on Geochemistry, vol. 4, edited by: Holland, H. D. and Turekian, K. K., Treatise on Geochemistry, 341–378, https://doi.org/10.1016/b978-0-08-095975-7.00310-7, 2014.

Schoene, B., Guex, J., Bartolini, A., Schaltegger, U., and Blackburn, T. J.: Correlating the end-Triassic mass extinction and flood basalt volcanism at the 100 ka level, Geology, 38, 387–390, https://doi.org/10.1130/g30683.1, 2010a.

https://doi.org/10.5194/gchron-2022-19
Preprint. Discussion started: 26 July 2022

Schoene, B., Latkoczy, C., Schaltegger, U., and Günther, D.: A new method integrating high-precision U–Pb geochronology with zircon trace element analysis (U–Pb TIMS-TEA), Geochim. Cosmochim. Acta, 74, 7144–7159, https://doi.org/10.1016/j.gca.2010.09.016, 2010b.

Subbarao, E. C., Agrawal, D. K., McKinstry, H. A., Sallese, C. W., and Roy, R.: Thermal expansion of compounds of zircon structure, J. Am. Ceram. Soc., 73, 1246–1252, https://doi.org/10.1111/j.1151-2916.1990.tb05187.x, 1990.

Swanson-Hysell, N. L., Hoaglund, S. A., Crowley, J. L., Schmitz, M. D., Zhang, Y., and Miller, J. D.: Rapid emplacement of massive Duluth Complex intrusions within the North American Midcontinent Rift, Geology, 49, 185–189, https://doi.org/10.1130/g47873.1, 2020.

Takehara, M., Horie, K., Hokada, T., and Kiyokawa, S.: New insight into disturbance of U-Pb and trace-element systems in hydrothermally altered zircon via SHRIMP analyses of zircon from the Duluth Gabbro, Chem. Geol., 484, 168–178, https://doi.org/10.1016/j.chemgeo.2018.01.028, 2018.

Trachenko, K., Dove, M. T., and Salje, E. K. H.: Structural changes in zircon under α-decay irradiation, Phys. Rev. B, 65, 180102, https://doi.org/10.1103/physrevb.65.180102, 2002.

Váczi, T.: A new, simple approximation for the deconvolution of instrumental broadening in spectroscopic band profiles, Appl. Spectrosc., 68, 1274–1278, https://doi.org/10.1366/13-07275, 2014.

Váczi, T. and Nasdala, L.: Electron-beam-induced annealing of natural zircon: a Raman spectroscopic study, Phys. Chem. Mineral., 44, 389–401, https://doi.org/10.1007/s00269-016-0866-x, 2017.

Weber, W. J.: Radiation-induced defects and amorphization in zircon, J. Materials Res., 5, 2687–2697, 1990.

Widmann, P., Davies, J. H. F. L., and Schaltegger, U.: Calibrating chemical abrasion: Its effects on zircon crystal structure, chemical composition and U-Pb age, Chem. Geol., 511, 1–10, https://doi.org/10.1016/j.chemgeo.2019.02.026, 2019.

Yamada, R., Tagami, T., Nishimura, S., and Ito, H.: Annealing kinetics of fission tracks in zircon: an experimental study, Chem. Geol., 122, 249–258, https://doi.org/10.1016/0009-2541(95)00006-8, 1995.

Yamada, R., Murakami, M., and Tagami, T.: Statistical modelling of annealing kinetics of fission tracks in zircon; Reassessment of laboratory experiments, Chem. Geol., 236, 75–91, https://doi.org/10.1016/j.chemgeo.2006.09.002, 2007.

https://doi.org/10.5194/gchron-2022-19
Preprint. Discussion started: 26 July 2022

Zhang, M., Salje, E. K. H., Capitani, G. C., Leroux, H., Clark, A. M., Schlüter, J., and Ewing, R. C.: Annealing of alpha-decay damage in zircon: a Raman spectroscopic study, J. Phys. Condens. Matter, 12, 3131, https://doi.org/10.1088/0953-8984/12/13/321, 2000.